

FRAGMENTATION OF MOLECULAR IONS IN ULTRAFAST LASER
PULSES

by

Utuq Ablikim

B.S., Harbin Institute of Technology, China, 2009

A REPORT

submitted in partial fulfillment of the
requirements for the degree

MASTER OF SCIENCE

Department of Physics
College of Arts and Science

KANSAS STATE UNIVERSITY
Manhattan, Kansas

2015

Approved by:

Major Professor
Itzik Ben-Itzhak

Abstract

Imaging the interaction of molecular ion beams with ultrafast intense laser fields is a very powerful method to understand the fragmentation dynamics of molecules. Femtosecond laser pulses with different wavelengths and intensities are applied to dissociate and ionize molecular ions, and each resulting fragmentation channel can be studied separately by implementing a coincidence three-dimensional (3D) momentum imaging method.

The work presented in this master's report can be separated into two parts. First, the interaction between molecular ion beams and femtosecond laser pulses, in particular, the dissociation of CO^+ into $\text{C}^+\text{+O}$, is studied. For that purpose, measurements are conducted at different laser intensities and wavelengths to investigate the possible pathways of dissociation into $\text{C}^+\text{+O}$. The study reveals that CO^+ starts to dissociate from the quartet electronic state at low laser intensities. Higher laser intensity measurements, in which a larger number of photons can be absorbed by the molecule, show that the doublet electronic states with deeper potential wells, e.g. $A^2\Pi$, contribute to the dissociation of the molecule.

In addition, the three-body fragmentation of CO_2^+ into $\text{C}^+\text{+O}^+\text{+O}^+$ is studied, and two breakup scenarios are separated using the angle between the sum and difference of the momentum vectors of two O^+ fragments.

In the second part, improvements in experimental techniques are discussed. Development of a reflective telescope setup intended to increase the conversion efficiency of ultraviolet (UV) laser pulse generation is described, and the setup is used in the studies of CO^+ dissociation described in this report. The other technical study presented here is the measurement of the position dependence of timing signals picked off of a microchannel plate (MCP) surface. The experimental method is presented and significant time spread over the surface of the MCP detector is reported [1].

Table of Contents

Table of Contents	iii
List of Figures	v
Acknowledgements	viii
Dedication	ix
1 Introduction	1
1.1 Our research focus	2
2 Experimental method and setup	3
2.1 Introduction	3
2.2 Coincidence 3D momentum imaging	3
2.2.1 Generating an ion beam	4
2.2.2 Laser beam alignment and characterization	5
2.2.3 Crossing the ion beam with the laser beam	6
2.2.4 Measuring fragmentation channels	7
2.3 Reflective telescope	7
2.3.1 Shrinking the IR beam size	8
2.3.2 Expanding the SH beam size	10
2.3.3 Harmonic generation performance	12
2.4 Three-body fragmentation analysis	13
2.4.1 Procedure for analyzing three-body fragmentation channels	13
2.4.2 Molecular-frame conversion	16
2.5 Position dependence of time signals picked off a microchannel plate detector	18
2.5.1 Introduction	18
2.5.2 Position dependence of time signals picked off a microchannel plate detector	19
3 Dissociation of CO⁺ ions in a strong laser field	23
3.1 Introduction	23
3.2 Dissociation of CO ⁺ in a strong laser field	25
3.2.1 Brief introduction to transition rules	26
3.2.2 Low intensity - 3×10^{12} W/cm ²	26
3.2.3 Intermediate intensity - 6×10^{13} W/cm ²	30
3.2.4 High intensity - 3×10^{15} W/cm ²	33

4	Three-body fragmentation of CO_2^+ into $\text{C}^+\text{+O}^+\text{+O}^+$ in a strong laser field	38
4.1	Introduction	38
4.2	Symmetric and asymmetric breakup of CO_2^+ into $\text{C}^+\text{+O}^+\text{+O}^+$	41
5	Summary and outlook	44
	Bibliography	51

List of Figures

2.1	Coincidence 3D momentum imaging setup	4
2.2	Laser beam and ion beam crossing	6
2.3	Schematic figure of reflective telescope	8
2.4	Schematic figure of lens telescope	9
2.5	Reflective telescope for shrinking beam size	9
2.6	Simplified reflective telescope	10
2.7	Reflective telescope for expanding beam size	11
2.8	Picture of two reflective telescopes on a breadboard	11
2.9	Spectra of IR and SH beams	13
2.10	Coincidence TOF map	14
2.11	Rotated TOF_1 vs. TOF_{23} spectrum	14
2.12	CM distribution of $\text{C}^+ + \text{O}^+ + \text{O}^+$ channel	15
2.13	Schematic figure of momentum vectors in laser frame	16
2.14	Dissociation plane of $\text{C}^+ + \text{O}^+ + \text{O}^+$ channel	17
3.1	Schematics of CO Franck-Condon transition	24
3.2	The deflector setup and the coincidence TOF map of CO^+	25
3.3	A few doublet and quartet state potential energy curves of CO^+	27
3.4	KER and KER- $\cos\theta$ spectra of $\text{C}^+ + \text{O}$ channel with 393 nm, 53 fs laser pulse at $3 \times 10^{12} \text{ W/cm}^2$	28
3.5	Angular distribution of peak β and a $\sin^2\theta$ fit for KER: 0.49 – 0.63 eV	28
3.6	KER and KER- $\cos\theta$ spectra of $\text{C}^+ + \text{O}$ channel with 786 nm, 30 fs laser pulse at $1 \times 10^{13} \text{ W/cm}^2$	29
3.7	Angular distributions of peak δ and ϵ and their fit functions	29
3.8	KER and KER- $\cos\theta$ spectra of $\text{C}^+ + \text{O}$ channel of CO^+ dissociation in a 393 nm, 53 fs laser pulse at $6 \times 10^{13} \text{ W/cm}^2$	30
3.9	Angular distribution of peak ϕ generated in 393 nm and 786 nm laser pulses and their fit functions	31
3.10	KER and KER- $\cos\theta$ spectra of $\text{C}^+ + \text{O}$ channel with 786 nm, 30 fs laser pulse at $8 \times 10^{13} \text{ W/cm}^2$	31
3.11	The expected yield of dissociation from vibrational levels of $a^4\Sigma^+$ state to the $1^4\Pi$ state after absorbing one 393-nm photon	32
3.12	KER and KER- $\cos\theta$ spectra of $\text{C}^+ + \text{O}$ channel with 393 nm, 53 fs laser pulse at $3 \times 10^{15} \text{ W/cm}^2$	33
3.13	KER- $\cos\theta$ spectra of $\text{C}^+ + \text{O}$ channel with 393 nm, 53 fs laser pulse at intensities: $6 \times 10^{13} \text{ W/cm}^2$; $3 \times 10^{14} \text{ W/cm}^2$; $3 \times 10^{15} \text{ W/cm}^2$	34

3.14	Schematics of transitions for $A^2\Pi + 2\omega \rightarrow D^2\Pi$ and the angular distribution of KER peak χ and its fit function	35
3.15	KER and KER-cos θ spectra of C ⁺ +O channel with 786 nm, 30 fs laser pulse at 2.8×10^{15} W/cm ²	36
3.16	The angular distribution for KER: 0.9 – 1.34 eV in a 786 nm, 30 fs, 2.8×10^{15} W/cm ² laser pulse	36
4.1	Newton diagram of C ⁺ +O ⁺ +O ⁺ channel	39
4.2	Coincidence TOF map: CO ₂ ⁺	40
4.3	Schematics of symmetric and asymmetric breakup	41
4.4	The number of C ⁺ +O ⁺ +O ⁺ breakup events as a function of cos α	42
4.5	Dalitz plot of the C ⁺ +O ⁺ +O ⁺ channel	42
4.6	The yield of C ⁺ fragments as a function of the relative energy with respect to the total KER of the C ⁺ +O ⁺ +O ⁺ channel undergoing symmetric breakup	43

Acknowledgments

First of all I am grateful that I have the chance and the environment to study what I love and I hope to continue this enthusiasm for science and research in my future studies. I am thankful for my parents who raised me and taught me the importance of moral values that are precious and ever lasting. They always told me to learn to become a genuine person before aiming to be a man with knowledge and power. I believe in academic life, knowledge, hardwork, humility and sincerity will lead a person to success.

Throughout those years of study in the physics department of Kansas State University, I learned a lot of knowledge from many different people at different levels. Those include physics knowledge that I gained in classes and research in our group and more importantly non-academic lessons that will positively influence the rest of my life, and I am extremely appreciative to some people who taught me those lessons. I chose to come to K-State not only knowing that the institute has a leading program in atomic molecular and optical science, but also because of my understanding of the research and the email correspondence with professor Brett Esry in the most humble way as I remember. I am thankful for that trust and the inspiration that ultimately led me here.

I am thankful for my advisor professor Itzik Ben-Itzhak. He taught me valuable knowledge throughout those years of my stay in his group. I learned to think critically in research. The long hours we spend together in the lab figuring out experimental problems or simply debugging noise on detector signals, etc. had huge impact on my experiences and knowledge. I am appreciative of the physics and life lessons that I learned from my advisor.

Professor Kevin Carnes is always a very helpful person. He taught me the knowledge on programming in SpecTcl and also physics knowledge through discussions in the group. There are no words that I can explain and even if I fill out several pages of this report with acknowledgements about the people that I am appreciative of, such as Kevin, it wouldn't

weight as much as joyful memories both during work and outside of work that will last for a long time. I am thankful for professor Kevin about everything, except the nickname “Barney” which I really really don’t like.

I thank professor Artem for agreeing to be a committee and I am also thankful for a few very useful physics discussions with him.

There are a lot of people that I need to be thankful of, some of them have tremendous impact on my life, some gave me valuable advices some gave me inspiration and confidence. The best thing I can do is to put those people and their teachings in my deep memory, and help other people in the same way that I was helped whenever I have the chance.

The group members that I have worked with gave me a lot of good memories. I am really appreciative of Mohammed Zohrabi, who has been a nice coworker and senior student. He helped me with experiments and research. I am also thankful to other group members, Ben Berry, Bethany Jochim, Travis Severt and few other former group members, Nora G. Kling, Kelsie J. Betsch and Bishwanath Gaire.

I thank my wife Gulnaz Rexit, she was with me at every difficult as well as the joyful moments. She experienced together the ups and downs in my life and I love her much more for giving me the best meditation when I am in dark by talking to me and by encouraging me.

Most importantly, I thank Allah for giving me the peace in my heart and calm in my mind. I pray for His kindness and forgiveness in my life and I will try my best to become that genuine person that I ought to be.

This work was supported by the Chemical Sciences, Geosciences, and Biosciences Division, Office of Basic Energy Sciences, Office of Science, U.S. Department of Energy.

Dedication

This work is dedicated to my father, my role model Ablikim Hasan, and to my caring and loving mother Turnisa Niyaz. Without their support and encouragement, I wouldn't be what I am and where I am today. I also dedicate the work to my beloved wife Gulnaz Rexit, who has been beside me and supportive of me in the ups and downs of my life. Last but not least, this dedication is to my little baby son Arslan. U. Ögen who is yet to open his eyes to this world.

Chapter 1

Introduction

Over the scope of the last century, studies on light-matter interactions have led to an understanding of structures and properties of atoms and molecules. Advances in ultrafast laser technology have made possible the study of atomic and molecular dynamics through interaction with intense laser pulses [2, 3]. The key idea behind using ultrashort laser pulses is to reach the nuclear (10^{-15} seconds: femtosecond) and electronic (10^{-18} seconds: attosecond) motion time scales in molecules. The intensities achieved by focused laser pulses can be comparable to electronic binding energies, and electrons in atoms and molecules can thus be removed by such laser pulses. As compared to atoms, tracing dynamics in diatomic and polyatomic molecules with strong laser pulses provides richer knowledge due to their complex structure and additional degrees of freedom, e.g. vibration and rotation. By examining the interactions of laser pulses with diatomic and polyatomic molecules, inherent properties of the molecules can be revealed.

In addition to advances in laser technology, molecular imaging techniques are also important in studying molecules. Many imaging methods, e.g. two-dimensional momentum imaging [4], coincidence three-dimensional (3D) momentum imaging [5, 6], cold-target recoil ion momentum spectroscopy (COLTRIMS) [7], and velocity-map imaging (VMI) [8], have been developed to study the interaction between ultrafast intense laser pulses and molecular targets in the gas phase and molecular ion beam targets.

1.1 Our research focus

In our group, research is mainly focused on the interaction between femtosecond laser pulses and molecular-ion beams. Investigations on dissociation and ionization dynamics of diatomic molecular ion beam targets ranging from the benchmark H_2^+ [5] ion to more complex systems, such as O_2^+ [9, 10], CO^+ [11], N_2^+ [12], and ND^+ [13], have previously taken place. For polyatomic molecules, we have studied the simplest triatomic system H_3^+ and its isotopes [14–18].

Using a previously developed 3D coincidence momentum imaging method in our group, in this master’s work I studied the dissociation of CO^+ into $\text{C}^+\text{+O}$ employing intense femtosecond laser pulses with wavelengths centered at 786 nm and 393 nm. The main goal behind the study was to understand the underlying fragmentation mechanism and to find possible dissociation pathways. In another study, preliminary results on the dissociation of triatomic CO_2^+ ions are presented, and the study is mainly focused on the $\text{C}^+\text{+O}^+\text{+O}^+$ breakup channel. An analysis method is introduced to separate symmetric (C-O bonds break symmetrically) and asymmetric (C-O bonds break asymmetrically) fragmentation events.

As examples of technical improvements of our experimental methods, a set of optical reflective telescopes for increasing the conversion efficiency of ultraviolet (UV) laser pulse generation is introduced, and the resulting high intensity laser pulses centered at 393 nm are used in the study of CO^+ dissociation. In addition, we studied the position dependence of timing signals picked off a large, e.g. $D=80$ mm, MCP detector. The results show significant time spread over the surface of the MCP, and our publication [1], which also describes the method used in this study, is included in Section 2.5.1.

Chapter 2

Experimental method and setup

2.1 Introduction

In the atomic, molecular and optical (AMO) science field, imaging the fragmentation processes of atoms and molecules is an important method for understanding laser-matter interactions. Coincidence 3D momentum imaging is one of the experimental techniques used to study molecular breakup dynamics [5, 9, 11, 12, 14, 16, 17, 19]. The experimental apparatus used in this technique was developed previously in professor Ben-Itzhak's group [5, 6, 20]. In the next section of this chapter, a brief review of the coincidence 3D momentum imaging method is given. Section 2.3 introduces a home-built reflective telescope that is used to (1) improve the conversion efficiency of 2nd and 3rd harmonic generation in non-linear processes in crystals and (2) to expand the harmonic beam size in order to achieve tighter focusing. Section 2.4 explains the method that is used to analyze three-body fragmentation channels. In the final Section 2.5, we introduce our published work on the position dependence of time signals picked off a microchannel plate detector [1].

2.2 Coincidence 3D momentum imaging

In the coincidence 3D momentum imaging technique, the major steps in an experiment are as follows: (1) generate the ions of interest in an electron cyclotron resonance (ECR) ion source, accelerate the ions and use ion optics to tune a collimated ion beam; (2) align a

laser beam and characterize the laser pulses; (3) cross the ion beam with the laser beam; (4) use the coincidence 3D momentum imaging setup shown in Figure 2.1 to measure the fragments. Comprehensive descriptions of the coincidence 3D momentum imaging technique and measurements can be found, for example, in references [20–23].

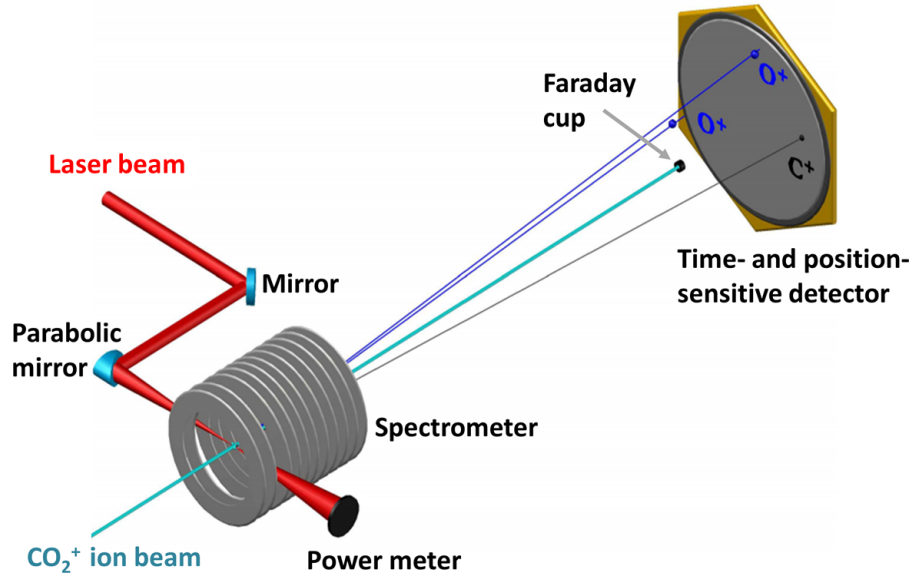


Figure 2.1: Schematic of the coincidence 3D momentum imaging setup used in the studies presented in this report

2.2.1 Generating an ion beam

Generating an ion beam is the starting point of the experiment. Usually, a specific molecular gas is continuously leaked into the ECR source which produces ions (both atomic and molecular) through fast electron impact ionization. This process involves a vertical transition from the initial neutral molecule to the molecular ion, and thus the vibrational population of the ions approximately follows the Franck-Condon distribution [24, 25]. By applying an electric field to accelerate the ions in the source, an ion beam with an energy range of 5-28 keV can be produced.

Along the ion beam path, an analyzing magnet and 4-jaw slits are implemented to select an ion beam of interest from among all the ion beams emerging from the source.

Faraday cups are installed at four different places along the beamline to monitor the ion beam current. Two electrostatic quadrupole lenses are used to collimate the ion beam, and deflectors in both horizontal and vertical directions are applied to point the ion beam in a certain direction. The final ion beam size is about $0.8 \times 0.8 \text{ mm}^2$. More details of the ion beamline can be found in the PhD theses of previous group members [11, 20–22]. Finally, the ion beam is collected in the last Farady cup (shown in Figure 2.1) in order to protect the detector from being damaged and to continuously monitor and record the ion current during the measurements in order to normalize experimental data sets.

2.2.2 Laser beam alignment and characterization

Ultrafast laser pulses are supplied by laser facilities in the James R. Macdonald Laboratory. Two laser systems, namely the Kansas Light Source (KLS) and PULSAR are used for the work presented in this report. Both of the systems are based on a Ti:Sapphire oscillator and a Ti:Sapphire multipass amplifier. The KLS generates linearly s-polarized 2 mJ laser pulses with a duration of 25-30 fs at around 780 nm central wavelength and a repetition rate of 2 kHz. PULSAR generates linearly p-polarized 2 mJ laser pulses with 21 fs pulse duration at a 10 kHz repetition rate, and the central wavelength is about 786 nm. Laser beams are transported to different experimental stations using flat reflective mirrors.

When laser pulses travel through air, there will be about 22 fs^2 group delay dispersion introduced into the pulse per meter of air, which will result in broadening of the laser pulse duration. In order to obtain Fourier transform limited (FTL) laser pulses at the interaction region, the grating position in the KLS or PULSAR laser system has to be adjusted to compensate for the additional chirp introduced through air travel as well as the chirp gained in any optical element in the laser path to the target.

A spectrometer is used to measure the wavelength distribution of the laser pulses and an SHG-FROG [26, 27] is used to measure the laser pulse duration. A power meter is used to measure the average laser power, and a CCD camera is employed in order to image the

laser focal size. By using the measured laser power, laser pulse duration and the focal spot size, we calculated the laser peak intensity using Equation 2.4. See more details on laser beam characterization in reference [21].

2.2.3 Crossing the ion beam with the laser beam

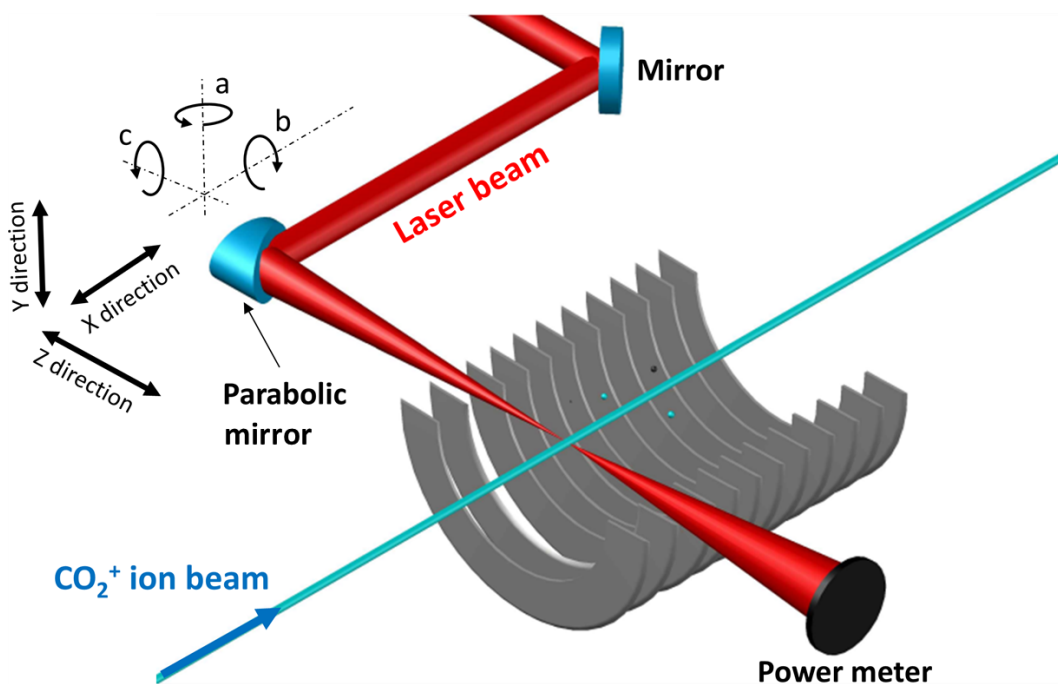


Figure 2.2: Schematic figure of the ion beam and laser beam crossing

In order to study laser-ion interactions, the ultrafast laser beam is focused onto the ion beam using an $f=203$ mm off-axis parabolic mirror [see Figure 2.2]. The parabolic mirror is mounted on a five-axis micrometer-driven stage where the mirror can be moved linearly in the x and y directions and rotated about the axes as shown by the arrows a, b and c in Figure 2.2. Then, the whole stage can be shifted in the z direction to move the focus of the laser beam relative to the ion beam axis. A static electric field is applied by a longitudinal spectrometer in order to separate ionic and neutral fragments by TOF. The fragments produced in the interaction region are detected by a multi-hit detector consisting of a multichannel plate and a delay-line anode and placed at the end of the apparatus.

The efficiency of detecting a fragment depends on the impact energy to some level. Hence, it's important to choose a proper ion beam energy together with the spectrometer voltage in order to detect fragments efficiently. However, the choice of ion beam energy is often a compromise between having reasonable fragment detection efficiency and obtaining high energy resolution for fragmentation channels.

2.2.4 Measuring fragmentation channels

All the fragments resulting from the interaction are detected in coincidence by a time- and position-sensitive detector [28]. Particular fragmentation channels are separated using a coincidence TOF map. All measurements are done in event mode, which means that the position and time information for each particle hitting the detector are recorded for each laser pulse. Using the time and position information for each fragment in a particular channel, the momentum of each fragment, the angular distributions between momentum vectors and laser polarization as well as the kinetic energy release of the channel can be calculated.

2.3 Reflective telescope

There are several experimental control parameters such as laser wavelength, pulse duration, laser intensity, etc. that can be modified in the experiment to help understand the fragmentation dynamics of molecules in a laser field. The fundamental infrared (IR) laser with 790 nm wavelength can be converted to a second harmonic (SH) laser beam with 395 nm and a third harmonic (TH) laser beam with 263 nm wavelength by using the sum frequency generation process [29]. Beta Barium Borate (BBO) crystals [30] are commonly used to generate second and third harmonic laser pulses. The details of SH and TH generation using BBO crystals are described, for example, in Mohammed Zohrabi's PhD thesis [21]. In this section, we focus on a method that allows us to increase the efficiency of harmonic beam generation as well as to increase the laser intensity of the harmonics.

Typically, the size of BBO crystals used in our lab to generate second harmonics is smaller than the size of the laser beam, so a collimated IR beam has to be shrunk in size in order to fully go through a BBO crystal. Another advantage of shrinking the IR beam size is that by increasing the intensity of the IR beam on the BBO crystal surface, a higher conversion rate of harmonic generation can be achieved. Moreover, one possible way to achieve high laser intensity is to expand the size of the SH beam. For this purpose, we developed two telescopes for shrinking the IR beam size as well as expanding the SH beam [see Figure 2.3].

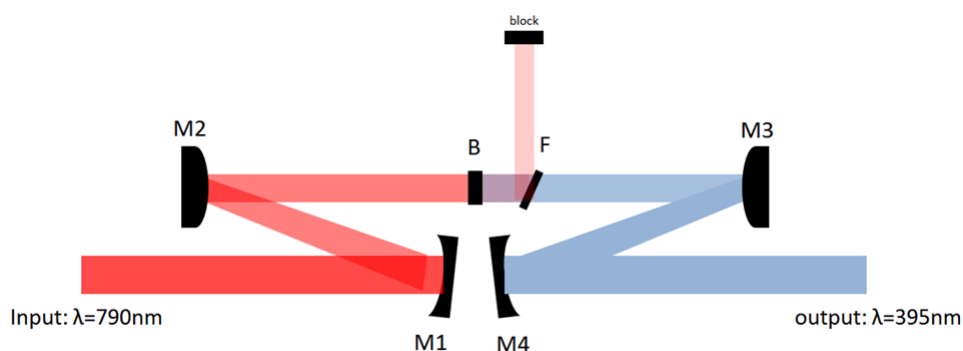


Figure 2.3: Schematic of reflective telescopes. **M1**: concave mirror $f=1000$ mm (coating: 600-1000 nm); **M2**: convex mirror $f=-500$ mm (same coating as **M1**); **B**: type-I BBO crystal; **F**: 1 mm separator to filter the IR beam by reflecting it to a beam block; **M3**: convex mirror $f=-500$ mm (coating: 390-410 nm); **M4**: concave mirror $f=1000$ mm (same coating as **M3**).

2.3.1 Shrinking the IR beam size

A combination of a concave and a convex lens are commonly used to shrink the size of a laser beam. For example, a collimated input laser beam with diameter D can be shrunk to a collimated beam with diameter d , as shown in Figure 2.4. The relation between the input and output beam sizes is as follows,

$$d = D \frac{f_2}{f_1}. \quad (2.1)$$

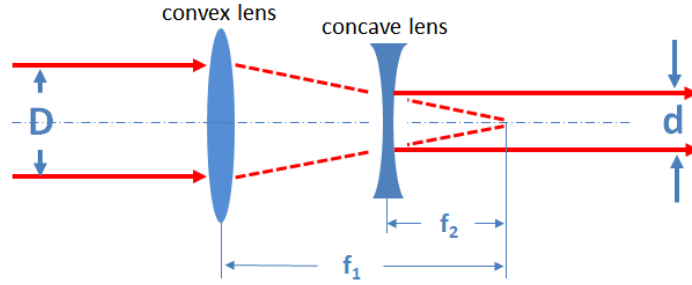


Figure 2.4: Schematic figure of a lens telescope. f_1 and f_2 are focal lengths of the convex and concave lenses, respectively.

Commonly used lenses have thicknesses on the order of a few millimeters and thus introduce considerable chirp in ultrashort laser pulses, as well as causing power loss due to absorption in the lens. Compared to lenses, however, mirrors with high reflective coatings can reduce power loss and will not introduce additional chirp to the laser pulses. For a telescope, a combination of a convex and a concave reflective mirror can do the job [see Figure 2.5].

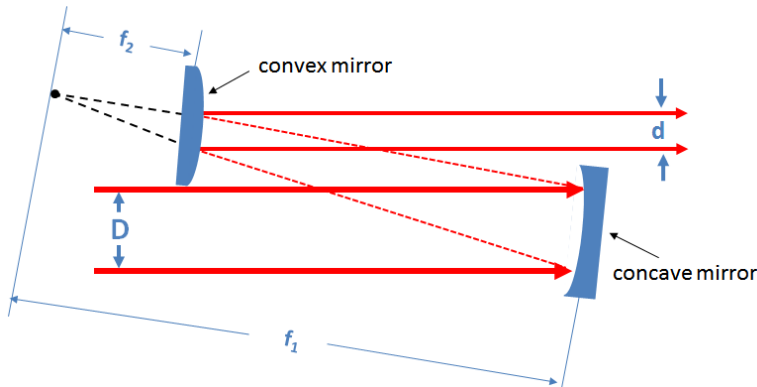


Figure 2.5: Schematic figure of a reflective telescope used to shrink the beam size; f_1 and f_2 are the focal lengths of concave and convex mirrors, respectively.

In the reflective telescope shown in Figure 2.5, the relation between input and output beam sizes is identical to the one given in Equation 2.1. However, proper incident angles should be chosen to reduce the beam distortion caused by spherical aberration. Details of the derivation for the proper angles of incidence are shown in reference [31], and the relation

between the incident angle θ_1 and the output angle θ_2 is reported as,

$$\theta_2 \approx \sqrt{\frac{f_1}{f_2} \frac{\theta_1}{|1 - \frac{b}{f_1}|}} \quad (2.2)$$

where b is the distance between the two mirrors and θ_1 and θ_2 are as described in the simplified Figure 2.6 below,

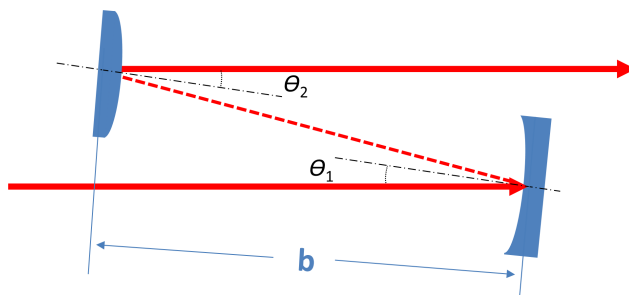


Figure 2.6: Simplified reflective telescope for shrinking beam size.

Note that the combination of a concave and a convex reflective mirror has to be used for a reflective telescope. The coating on the surface of both concave and convex mirrors in the telescope that is used to shrink the IR beam is highly reflective for the wavelength range 700 – 900 nm.

2.3.2 Expanding the SH beam size

The goal of expanding the SH beam is to achieve tight focus on the target. The relation between the beam size of the output UV beam D_0 and the size of the focus d_0 is

$$d_0 = \frac{2f\lambda}{D_0}, \quad (2.3)$$

where f is the focal length of the focusing element, which in our case is the off-axis parabolic mirror shown in Figure 2.1, and λ is the laser wavelength. From the equation, we know that the larger the input beam size D_0 , the tighter the focal spot d_0 , thus leading to a higher laser peak intensity

$$I = \frac{P}{f_{rep} A \Delta t}, \quad (2.4)$$

where I is the peak intensity, P is the laser average power, A is the laser focal area which, if we assume a Gaussian beam profile for the laser beam and do not consider astigmatism, can be written as $A = \pi(d_0/2)^2$, Δt is the laser pulse duration, and f_{rep} is the laser repetition rate.

In order to expand the SH beam, the same principle of a reflective telescope described in Section 2.3.1 is used, however the order of convex and concave mirrors are switched [see Figure 2.7]. The final size of the expanded SH beam needs to fit within the size of the laser transport mirror and the size of the parabolic mirror, and it can be calculated using Equation 2.1. Moreover, reflective coatings on the spherical mirrors are ultraviolet (UV) enhanced in order to reduce the laser power loss. Figure 2.8 is a picture of two reflective

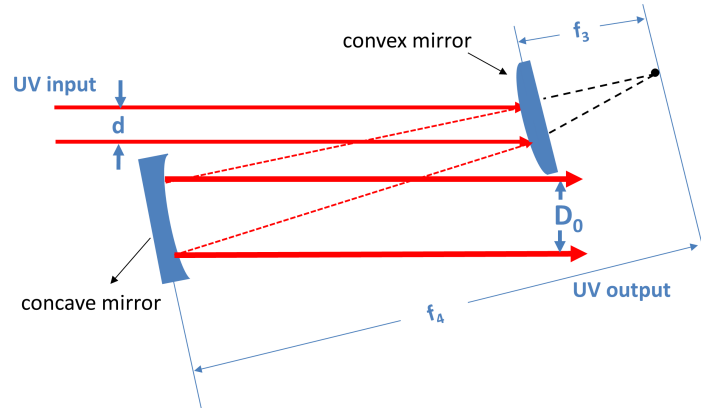


Figure 2.7: Schematic figure of expanding reflective telescope; f_3 and f_4 are the focal lengths of the convex and concave mirrors, respectively.

telescopes and the BBO crystal combined together in the lab to serve the purpose of both shrinking the IR beam and expanding the SH beam.

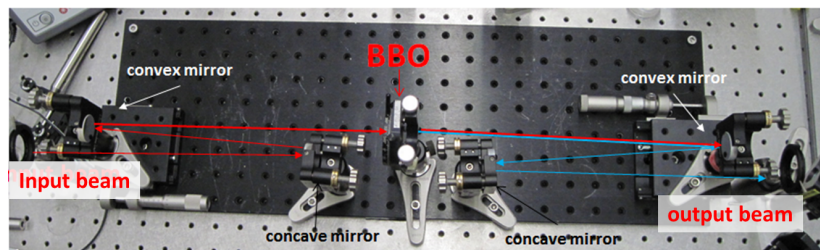


Figure 2.8: Picture of two reflective telescopes on a breadboard.

2.3.3 Harmonic generation performance

Table 2.1, shown below, includes the measured parameters of the IR and SH beams in our measurements. IR beam parameters are measured before the two reflective telescopes and the SH beam parameters are measured after the telescopes.

Beam Type	IR beam	SH beam
Laser power	11 W	4 W
Pulse duration	26 fs	53 fs
Laser bandwidth	36 nm	7 nm
Beam diameter	16 mm	15 mm

Table 2.1: Laser parameters: IR laser beam was measured before the two reflective telescopes and SH laser beam was measured after the telescopes

The duration of the IR laser pulse is measured using a FROG setup, and the SH laser pulse duration is measured with a SD-FROG setup [27]. Prior to the two reflective telescopes, by using a lens telescope as shown in Figure 2.4, the typical conversion rate from IR to SH in our old measurements was about 25% and the intensity of the SH beam could only reach to about 1×10^{14} W/cm². With the help of the reflective telescope setup shown in Figure 2.8, the conversion rate of IR to SH beam in our measurement has increased to 36%, and by expanding the SH beam size, the peak intensity of the SH beam has increased to 3×10^{15} W/cm². The increase in intensity is partly due to the higher conversion efficiency but mostly due to the tighter focus allowed by the beam expansion. The laser spectra of the input IR beam and the output SH beam are shown below in Figure 2.9.

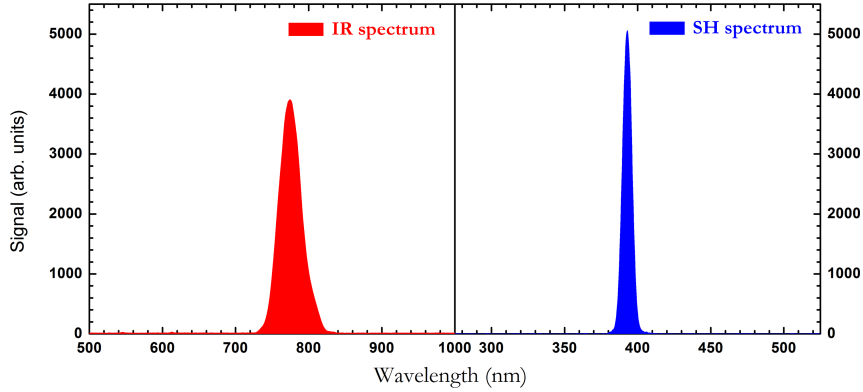


Figure 2.9: Spectra of IR and SH beams.

2.4 Three-body fragmentation analysis

2.4.1 Procedure for analyzing three-body fragmentation channels

Laser-induced two-body breakup of diatomic and triatomic molecular ions has been studied extensively by our group using coincidence 3D momentum imaging techniques [5, 9, 10, 12–14, 17, 19, 32–34]. Comprehensive explanations of the two-body fragmentation measurements and our analysis method have been introduced previously [20, 22]. The results from experiments on the three-body fragmentation of the benchmark H_3^+ system and its isotopes [14–18] have been published by our group, and the three-body analysis method was developed [15, 18, 22]. In this work, a few modifications are made in the analysis procedure.

First, three-body fragmentation channels are separated using a coincidence TOF map as shown in Figure 2.10. By plotting the yield as a function of the TOF of the 1st hit and the TOF of the center of mass (CM) of the second and third hits, the three-body channels appear as narrow strips due to conservation of momentum along the ion beam axis direction. The expression for TOF_{23} is

$$\text{TOF}_{23} = \frac{m_2 \times \text{TOF}_2 + m_3 \times \text{TOF}_3}{m_2 + m_3}, \quad (2.5)$$

where TOF_2 and TOF_3 are the TOF of the second and third hits, respectively. Note that, in the first step, the parameters m_1 , m_2 and m_3 are set using the masses of the C and the O fragments, M_C and M_O , e.g. $m_1 = m_2 = M_O$ and $m_3 = M_C$.

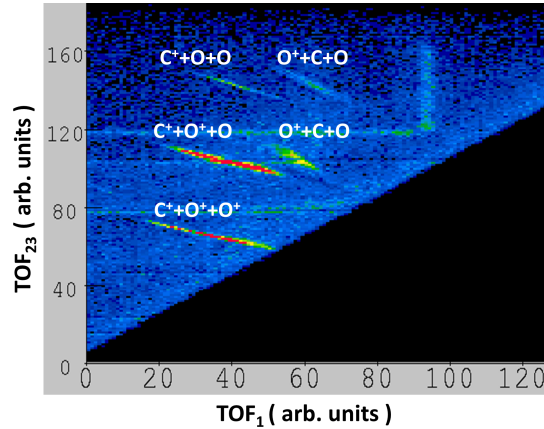


Figure 2.10: Coincidence TOF map of three-body fragmentation of CO_2^+ induced by 26 fs linearly polarized laser pulses with $6.5 \times 10^{15} \text{ W/cm}^2$. The three-body breakup channels appear as narrow “lines” in this map due to momentum conservation along the ion beam direction.

The next step is selecting a channel of study in the TOF coincidence map shown in Figure 2.10. Then, the mass parameters m_1 , m_2 and m_3 are set according to the TOF of fragments in the selected channel in the order of short to longer TOF, e.g. for the $\text{C}^+ + \text{O}^+ + \text{O}^+$ channel, $m_1 = M_{\text{C}^+}$ and $m_2 = m_3 = M_{\text{O}^+}$, where M_{C^+} and M_{O^+} are the masses of C^+ and O^+ , respectively. By rotating the selected TOF coincidence stripe, e.g. the $\text{C}^+ + \text{O}^+ + \text{O}^+$ channel, vertical and horizontal time gates can be set to separate pure triple coincidence events from random coincidences [see Figure 2.11].

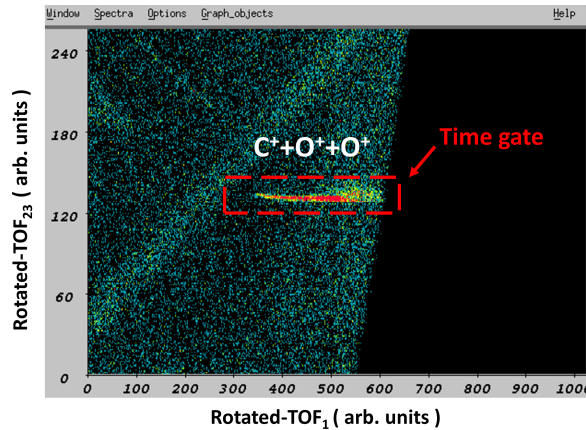


Figure 2.11: Rotated coincidence TOF stripe of the $\text{C}^+ + \text{O}^+ + \text{O}^+$ channel. The red dashed box represents the time gate set on the channel in order to reduce random coincidences.

In order to further clean the data, the x and y CM of events that passed the coincidence TOF gate in the previous step are calculated and a position gate is applied to extract triple coincidence events [see Figure 2.12]. The expression of CM in the x and y directions are,

$$X_{CM} = \frac{m_1 \times x_1 + m_2 \times x_2 + m_3 \times x_3}{m_1 + m_2 + m_3} \quad (2.6)$$

$$Y_{CM} = \frac{m_1 \times y_1 + m_2 \times y_2 + m_3 \times y_3}{m_1 + m_2 + m_3}, \quad (2.7)$$

where x_1, x_2, x_3 and y_1, y_2, y_3 are the measured positions of the three fragments. Note that in both equations above, the measured positions of the three fragments are used. Since these hits occur at different times, an approximation is made by assuming that the positions don't change much between the common center of mass time and the three individual times.

In order to calculate the CM positions of the system accurately, the time dependence of positions for each fragment needs to be included in future development of the analysis method.

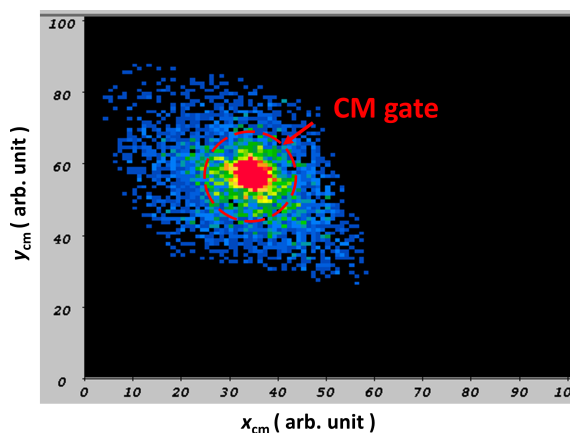


Figure 2.12: Center of mass, $x_{cm} - y_{cm}$ distribution of the $C^+ + O^+ + O^+$ channel. The red dashed circle represents the CM position gate applied in order to reduce random coincidence.

Finally, using time and position information of the three fragments, the momentum of each fragment in the molecular frame is calculated. From these momentum vectors, we evaluate the quantities of interest, such as kinetic energy release (KER) and angular distributions.

2.4.2 Molecular-frame conversion

To understand molecular dynamics in both two- and three-body fragmentation requires one to study distributions of momentum and energy in the molecular frame of reference. As explained in the previous section, the measured momentum vectors of all fragments are evaluated in the molecular frame. This is the \mathbf{i} , \mathbf{j} , \mathbf{k} frame moving with the center of mass velocity of the molecule, where \mathbf{i} is parallel to the ion beam, \mathbf{j} is the propagation direction of the laser, and \mathbf{k} is the laser polarization direction [see Figure 2.13]. This section explains the conversion from the molecular frame to the molecular dissociation frame, which for three-body breakup is two dimensional. For example, momenta of C^+ , $\text{O}_{(1)}^+$ and $\text{O}_{(2)}^+$ in the molecular frame, \mathbf{P}_{C^+} , $\mathbf{P}_{\text{O}_{(1)}^+}$ and $\mathbf{P}_{\text{O}_{(2)}^+}$, are shown as vectors in Figure 2.13. We denote \hat{n} as the unit vector normal to the molecular dissociation plane.

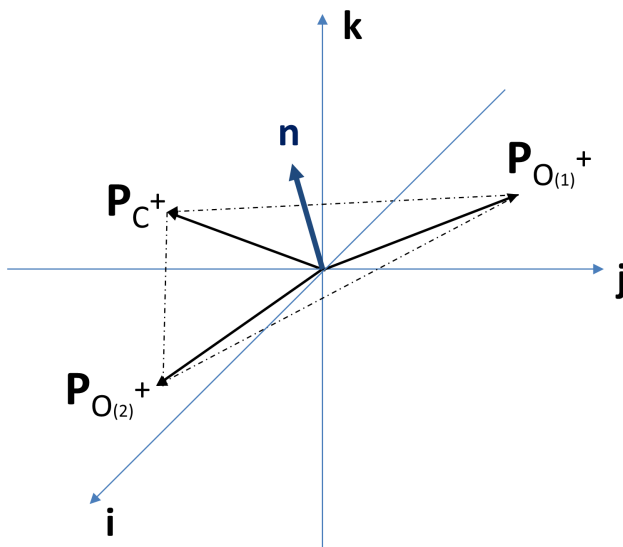


Figure 2.13: Schematic figure of momentum vectors for the three fragments in the $\text{C}^+ + \text{O}^+ + \text{O}^+$ channel in the molecular frame. Coordinates shown in this figure are, \mathbf{k} : laser polarization direction, \mathbf{j} : laser propagation direction, and \mathbf{i} : parallel to the ion beam.

By choosing the $\text{O}_{(1)}^+$ fragment momentum to be along the x axis, the molecular dissociation frame can be constructed with the following three unit vectors,

$$\hat{n} : \frac{(\mathbf{P}_{\text{C}^+} - \mathbf{P}_{\text{O}_{(1)}^+}) \times (\mathbf{P}_{\text{O}_{(2)}^+} - \mathbf{P}_{\text{O}_{(1)}^+})}{|\mathbf{P}_{\text{C}^+} - \mathbf{P}_{\text{O}_{(1)}^+}| |\mathbf{P}_{\text{O}_{(2)}^+} - \mathbf{P}_{\text{O}_{(1)}^+}|}. \quad (2.8)$$

$$\hat{x} : \frac{\mathbf{P}_{O(1)+}}{|\mathbf{P}_{O(1)+}|} \quad (2.9)$$

$$\hat{y} : \hat{n} \times \hat{x} \quad (2.10)$$

The momentum vectors of the three fragments \mathbf{P}'_{C^+} , $\mathbf{P}'_{O(1)+}$ and $\mathbf{P}'_{O(2)+}$ in the molecular dissociation frame can be calculated by projecting the $\mathbf{P}_{C^+}^+$, $\mathbf{P}_{O(1)+}^+$ and $\mathbf{P}_{O(2)+}^+$ vectors into the $\hat{x}\hat{y}\hat{n}$ frame,

$$\begin{aligned} \mathbf{P}'_{C^+x} &= \mathbf{P}_{C^+} \cdot \hat{x} & \mathbf{P}'_{O(1)+x} &= \mathbf{P}_{O(1)+} \cdot \hat{x} & \mathbf{P}'_{O(2)+x} &= \mathbf{P}_{O(2)+} \cdot \hat{x} \\ \mathbf{P}'_{C^+y} &= \mathbf{P}_{C^+} \cdot \hat{y} & \mathbf{P}'_{O(1)+y} &= \mathbf{P}_{O(1)+} \cdot \hat{y} & \mathbf{P}'_{O(2)+y} &= \mathbf{P}_{O(2)+} \cdot \hat{y} \end{aligned}$$

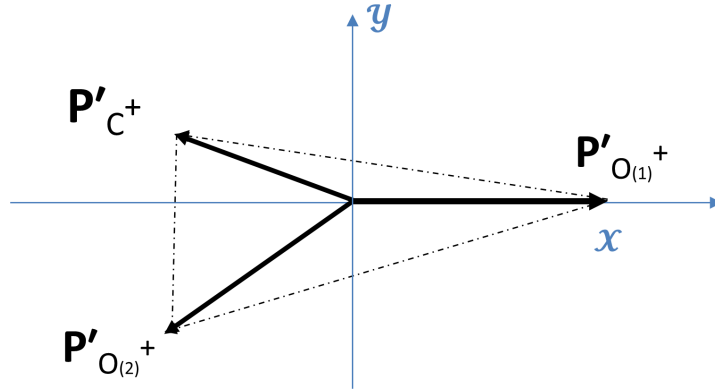


Figure 2.14: Molecular dissociation plane of the $C^+ + O^+ + O^+$ channel.

Figure 2.14 presents the momentum vectors of the fragments in the xy -plane. We normalize the sizes of all three vectors in Figure 2.14 by the size of $\mathbf{P}'_{O(1)+}$ and make sure that the C^+ fragment momentum is always in the upper half of the plane (e.g. $\mathbf{P}'_{C^+} > 0$) and the other O^+ momentum is in the lower half half of the plane ($\mathbf{P}'_{O^+} < 0$). By doing so, we can obtain a Newton diagram of the three-body fragmentation channel $C^+ + O^+ + O^+$.

The Newton diagrams using the molecular dissociation frame momentum vectors described above are not included in this report. The purpose of the section is to present the method for future studies of the fragmentation of polyatomic molecules.

2.5 Position dependence of time signals picked off a microchannel plate detector

2.5.1 Introduction

The coincidence 3D momentum imaging measurements described in the next chapters are performed using a multi-hit imaging detector that consists of a chevron stack of microchannel plates (MCP) and a hex delay-line anode detector. This detector assembly allows us to measure the time and position information for fragments resulting from the laser and ion interaction. The ability to obtain time and position information of the fragments with improved precision will lead to correspondingly higher momentum and energy resolutions that are important for understanding the fragmentation processes. As a specific example relating to the work in this report, namely our studies on CO^+ dissociation, if we are able to attain vibrational resolution in the KER spectrum, it may become easier to identify the underlying mechanism causing the dissociation.

Previous efforts have been made to characterize the temporal resolution of MCP detectors [35–37]. A practical question, however, is the following: for large MCPs, does the time signal depend on the position of the particle hit? That is, does surface propagation have a notable effect on time signals picked off an MCP? To our knowledge, this question has not been investigated previously. As we demonstrate in the next section, the broadening caused by the position dependence of timing signals is comparable to the temporal resolution of our imaging detector. Hence, this phenomenon cannot be simply ignored.

In order to characterize such a dependence, however, UV pulses with a much shorter time scale than the temporal resolution must be used to avoid convolution caused by the contribution of laser pulse duration. Moreover, to activate the MCP detectors, a UV photon with higher energy than the MCP surface work function is required. In the present case, applying the reflective telescope described in Section 2.3.1, third harmonic laser pulses with 262 nm central wavelength and estimated pulse duration of 90 fs are ideal candidates for studying the time broadening.

2.5.2 Position dependence of time signals picked off a microchannel plate detector

Note: Position dependence of time signals picked off a microchannel plate detector

U. Ablikim, M. Zohrabi, Bethany Jochim, B. Berry, T. Severt, K. D. Carnes, and I. Ben-Itzhak, *Rev. Sci. Instrum.* **86**, 016111 (2015).



Note: Position dependence of time signals picked off a microchannel plate detector

U. Ablikim, M. Zohrabi, Bethany Jochim, B. Berry, T. Severt, K. D. Carnes, and I. Ben-Itzhak^{a)}

J. R. Macdonald Laboratory, Physics Department, Kansas State University, Manhattan, Kansas 66506, USA

(Received 12 December 2014; accepted 8 January 2015; published online 20 January 2015)

Using an ultrafast laser and a precision mask, we demonstrate that time signals picked off directly from a microchannel plate detector depend on the position of the hit. This causes a time spread of about 280 ps, which can affect the quality of imaging measurements using large detectors. © 2015 AIP Publishing LLC. [<http://dx.doi.org/10.1063/1.4906327>]

The use of multi-hit detectors that provide time and position information for each of a few particles created in a single event is widespread across many disciplines, ranging from atomic, molecular, and optical (AMO) physics^{1–3} to nuclear physics,⁴ particle physics, and space instrumentation,⁵ as well as other fields.⁶ In many of these detectors, a stack of microchannel plates (MCPs) is used to convert the single particle hit (including photons) into an electron “cloud” producing a large enough signal to be detected.⁷ Many decoding schemes have been used to measure the position information of each particle in such detectors, including resistive anodes,⁸ backgammon anodes,⁹ delay-line anodes,¹⁰ and phosphor screens coupled with a CCD (or CMOS) camera.^{11,12} The time signal in most cases is directly measured from the front or back side of the MCP stack.^{7,10,13}

Microchannel plate detectors can achieve “ultra-high time resolution (<100 ps).”⁷ However, as the diameter of these MCP detectors used in imaging applications increases, one may wonder if this time resolution is affected by the propagation time on the detector surface when the timing signal is picked off directly from the MCP surface. This time can be estimated to be at least 100 ps for a signal originating 30 mm away from the pickup if one assumes that the charge signal propagates at the speed of light. Using a more realistic velocity factor¹⁴ of 0.5 will yield 200 ps for the same signal. Given that 80 and 120 mm diameter MCP detectors are commonly used suggests time spreads of the order of 250 and 400 ps, respectively.

In this work, we are addressing exactly this question, namely, what is the time broadening caused by hits across the MCP surface? In other words, we determine the position dependence of the time signals picked off directly from the MCP back surface. To accomplish this goal, a MCP detector with a delay-line anode was illuminated through a regular mask by about 90 fs laser pulses—effectively instantaneous in comparison to the signal propagation time across the MCP. Employing a similar ultrafast laser beam technique, the time resolution of a MCP has been determined to be 200–300 ps, depending on the voltage applied across the MCP.¹⁵ It is important to note that in that study,¹⁵ only a small spot was illuminated, and the time signal was picked off

from an impedance-matched anode.^{7,16} Therefore, the issue of propagation of the charge signal on the MCP surface remains to be studied. This question is important when using position-sensitive anodes and picking off the time signal directly from the MCP front or back surface. In the results presented below, it is shown that time-broadening is due in large part to the position dependence of the time signal taken directly from the MCP. Moreover, the measured values are consistent with the pulse-propagation estimates above. The impact of this “time dependence on position” on reducing electronic noise affecting the position signals of such detectors and on lost-signal reconstruction is also briefly discussed.

As mentioned above, we have used an ultrafast laser providing about 2 mJ pulses centered at 787 nm (with a 28 nm bandwidth) at a repetition rate of 2 kHz. To activate the MCP efficiently, a higher energy photon is needed^{7,17}—in an earlier study,¹⁵ 267 nm pulses worked well. To that end, we generated 262 nm pulses through third harmonic generation using two type-I beta-barium borate (BBO) crystals, as described in detail by Zohrabi¹⁸ and others.^{19,20} This 262 nm laser beam is directed toward the detector through a diverging lens and a flat mirror such that it illuminates the whole detector, as shown in Fig. 1(a). A mask with regular circular holes (0.78 mm in diameter) spaced by 5 mm (center to center) and placed a few mm in front of the detector defined the x, y position on the detector surface, as shown in Fig. 1(b).

The detector used in this study consists of a pair of 80 mm diameter MCPs (chevron assembly⁷) coupled with a RoentDek¹³ hex delay-line anode. The position information is determined from the time difference between signals arriving at both ends of each wire.^{10,13} The time information is evaluated from a charge signal picked off directly from either the front or back surface of the MCP stack.^{7,10,13} Since they are similar, we show only back surface results here.

A photodiode exposed to a small fraction of the laser beam provides the start signal for a multi-hit, multi-channel time-to-digital converter (TDC, CAEN V1290N) while the time signals from the MCP back surface are used as the stop. The MCP signals were amplified by a pre-amplifier (ORTEC VT-120B), and a constant-fraction discriminator (CFD, ORTEC 935) was used to generate the standard Nuclear Instrumentation Module (NIM) signal needed by the TDC. The TDC resolution is about 25 ps, i.e., better than that of

^{a)}Electronic mail: ibi@phys.ksu.edu.

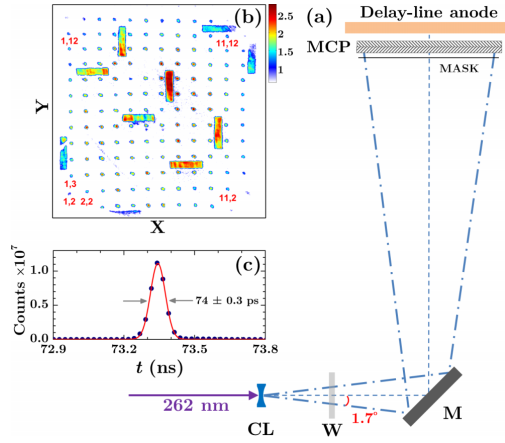


FIG. 1. Experimental schematic: (a) schematic of the setup used for testing an 80 mm MCP with about 90 fs pulses at 262 nm, where CL—concave lens, W—window, and M—mirror. (b) The mask used to define the position, having a regular array of small holes 5 mm center-to-center. (c) The time-difference spectrum of a photodiode start—photodiode stop measurement used to determine the electronic broadening to be about $74/\sqrt{2} \sim 50$ ps.

the MCP. Moreover, the 262 nm chirped laser pulses are estimated to be about 90 fs long, practically instantaneous on the response time scale of the MCP. In principle, any sub 25 ps pulsed laser can be used to reproduce the present detector test if it provides energetic enough photons. The time-broadening caused by the photo-diode and timing electronics was measured to be about 50 ps by using an identical photodiode to generate the stop signal instead of the MCP [see Fig. 1(c)].

The photon flux (i.e., laser intensity) was kept low enough to keep the counting rate at about 200 Hz on average, a photon-hit probability smaller than 0.1 per pulse, to reduce multiple-photon hits on the detector and their effect on the time-position correlation. The data were recorded event-by-event, enabling offline analysis, which includes the elimination of the small fraction of multi-hit events. Moreover, this allows the analysis of the time signals of events originating from specific holes or a row or column of holes, therefore mapping the position dependence of the MCP time signal.

The main finding of our study is that the time signal picked off a MCP back surface depends on the position of the particle's (photon in this case) hit on the detector. This effect causes a time spread of about 280 ps over the whole detector, defined as the maximum difference between the centroids of the time distributions for all holes. In Fig. 2(a), we present the time distributions associated with a few well-defined 0.78-mm circular holes along the detector center, which clearly show that the time shift from one position to another is a significant contribution to the time broadening. This time dependence on position is further illustrated in Figs. 2(b) and 2(c), which show the centroid of the time distribution $\langle t_{i,j} \rangle$ relative to the shortest measured time $\langle t_{2,8} \rangle$ at specific positions on the MCP detector defined by the mask holes (i,j) . This effect is expected to become the limiting factor as other sources of time broadening, like electronics, are improved further.

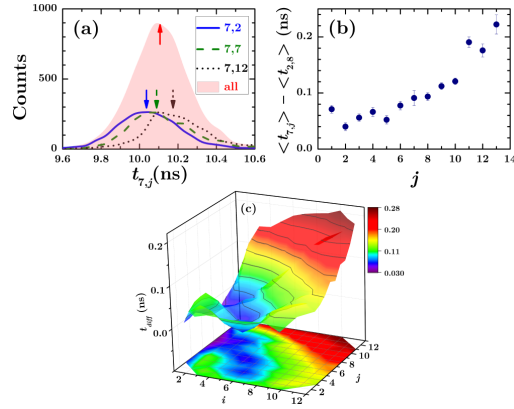


FIG. 2. Position dependence of time signals: (a) time distributions (with scaled peak value) for a few holes along a column near the detector center (the centroid of each, $\langle t_{i,j} \rangle$, evaluated by a Gaussian fit is marked by an arrow). Also shown is the distribution for all holes—scaled to fit. The deviation of $\langle t_{i,j} \rangle$ from $\langle t_{2,8} \rangle$, the shortest time, is shown in (b) along the same column shown in (a), and (c) the whole detector—a smoothed surface plot.

The time dependence on position, $t(x,y)$, follows the expected trend of longer times for particles (i.e., photons) hitting the MCP further from the connection of the pick-off wire, which is near $i,j = 7,1$, as shown for the mask column with $i = 7$ in Fig. 2(b). However, the complete distribution on the detector suggests that charge signal propagation along the MCP surface cannot be the whole story, as that would suggest a similar time for $i,j = 2,6$ and $12,6$, which is clearly not the case according to Fig. 2(c). The most likely reason is signal propagation along the conducting surface of the ceramic ring holding the MCP stack, which can provide a faster route for charge signals from these specific points to the pick-off wire. The fact that this route reduces the time for $i,j = 2,6$ but not for $i,j = 12,6$ is most likely due to the better contact of the ceramic ring on one side of the stack than the other. Moreover, this may also explain why the lowest time is near $i,j = 2,8$, where one of the stacking clips is attached, and not next to the pick-off wire as expected. Further work is needed to understand the complex time dependence on position, to model $t(x,y)$, and to try to reduce its impact by improving the contact and conductivity of the rings holding the MCP stack together. However, this goes beyond the scope of this work.

This time dependence on position might have significant consequences on imaging MCP detectors as they get larger and their resolution improves. For example, if a three-dimensional velocity image is desired, then the time dependence on position may distort the image by affecting the velocity component perpendicular to the detector plane. This is particularly important when imaging electrons, for which short time-of-flights are typical.³ At present, the use of meshes in front of imaging detectors typically causes larger distortions than $t(x,y)$.

Another example where $t(x,y)$ may have an impact is on the MCP detector using a delay-line anode, like the detector used here. In a delay line, the position is determined from the

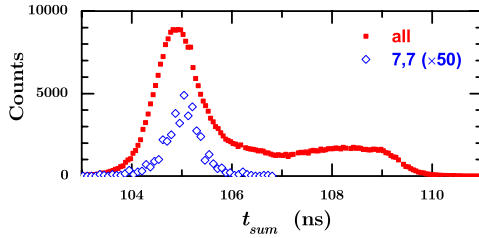


FIG. 3. Time-sum distribution for one of the wires of the delay-line anode, which is aligned 15° relative to the x -axis. Note that the distribution at a specific location ($i, j = 7, 7$) is significantly narrower than the one including the contributions from all holes—a broadening that limits electronic noise suppression on the delay-line decoder (see text).

time difference between the signals arriving at the two ends, t_1 and t_2 . It is convenient to also define the time sum, as it is expected to be constant

$$t_{sum} = (t_1 - t_i) + (t_2 - t_i) = L/v_s, \quad (1)$$

where t_i is the time the charge cloud of the MCP hits the delay-line wire of length L , and v_s is the signal speed on that wire.

According to Eq. (1), the time-sum spectrum, like the one shown in Fig. 3, should exhibit a single narrow peak. In practice, this spectrum is typically noisy, but the noise can be greatly suppressed by accepting only t_1 and t_2 signal pairs for which the time sum falls in a narrow “gate” centered around the expected value. Figure 3 clearly indicates that the time-sum peak associated with a specific position on the detector is much narrower than for the whole detector. The position dependence of t_i in Eq. (1) contributes about 0.5 ns to the width of the measured t_{sum} distribution, shown in Fig. 3, and clearly other sources contribute too. Reducing the width of the t_{sum} peak will ultimately improve the signal to noise of delay line detectors.

More importantly, Eq. (1) is commonly used to “reconstruct lost signals,”²¹ for example, one can compute $t_2 = t_{sum} - t_1 + 2t_i$ (using $\langle t_{sum} \rangle$ of the distribution) in cases where a t_2 signal is missing. Clearly, the computed t_2 accuracy will be reduced, by about 0.5 ns in our case, because of the position dependence of t_i . Modeling of $t(x, y)$ may, therefore, improve the reconstructed events in imaging measurements using delay-line detectors.

In summary, a method for measuring the position dependence of time signals picked off a MCP surface is

presented. A time spread of about 280 ps was measured for an 80 mm MCP detector—large enough to affect imaging measurements and expected to increase with MCP size.

The authors acknowledge V. Kumarappan’s group for assistance with the KLS laser beam. This work was supported by the Chemical Sciences, Geosciences, and Biosciences Division, Office of Basic Energy Sciences, Office of Science, U.S. Department of Energy. The MCP detector used for this work was provided by the National Science Foundation under Award No. IIA-1430493. B.J. is supported by the Department of Energy Office of Science Graduate Fellowship Program (DOE SCGF), made possible in part by the American Recovery and Reinvestment Act of 2009, administered by ORISE-ORAU under Contract No. DE-AC05-06OR23100.

- ¹I. Ben-Itzhak, in *Fragmentation Processes: Topics in Atomic and Molecular Physics*, edited by C. T. Whelan (Cambridge University Press, Cambridge, 2013).
- ²B. J. Whitaker, *Imaging in Molecular Dynamics: Technology and Applications (A User’s Guide)* (Cambridge University Press, 2003).
- ³J. Ullrich, R. Moshhammer, A. Dorn, R. Dörner, L. P. H. Schmidt, and H. Schmidt-Böcking, *Rep. Prog. Phys.* **66**, 1463 (2003).
- ⁴A. S. Tremsin, W. B. Feller, and R. G. Downing, *Nucl. Instrum. Methods Phys. Res., Sect. A* **539**, 278 (2005).
- ⁵*Observing Photons in Space: A Guide to Experimental Space Astronomy*, 2nd ed., edited by M. C. E. Huber, A. Pauluhn, J. L. Culhane, J. G. Timothy, K. Wilhelm, and A. Zehnder (Springer, 2013), Vol. 9.
- ⁶B. Seitz, *J. Instrum.* **7**, C01031 (2012).
- ⁷J. L. Wiza, *Nucl. Instrum. Methods* **162**, 587 (1979).
- ⁸W. P. Acker, B. Yip, D. H. Leach, and R. K. Chang, *J. Appl. Phys.* **64**, 2263 (1988).
- ⁹R. Ali, V. Frohne, C. L. Cocke, M. Stockli, S. Cheng, and M. Raphaelian, *Phys. Rev. Lett.* **69**, 2491 (1992).
- ¹⁰O. Jagutzki, A. Cerezo, A. Czasch, R. Dörner, M. Hattaf, M. Huang, V. Mergel, U. Spillmann, K. Ullmann-Pfleger, T. Weber, H. Schmidt-Böcking, and G. D. W. Smith, *IEEE Trans. Nucl. Sci.* **49**, 2477 (2002).
- ¹¹L. Dinu, A. T. J. B. Eppink, F. Rosca-Pruna, H. L. Offerhaus, W. J. van der Zande, and M. J. J. Vrakking, *Rev. Sci. Instrum.* **73**, 4206 (2002).
- ¹²N. G. Kling, D. Paul, G. Laurent, S. De, H. Li, Z. Wang, B. Ahn, C. H. Kim, T. K. Kim, I. V. Litvinyuk, C. L. Cocke, I. Ben-Itzhak, D. Kim, and M. F. Kling, *J. Instrum.* **9**, P05005 (2014).
- ¹³RoentDek Handels GmbH, <http://www.roentdek.com>.
- ¹⁴Velocity factor is defined as the ratio between the pulse speed in the medium and the speed of light in vacuum.
- ¹⁵Q. Zhang, K. Zhao, and Z. Chang, *Rev. Sci. Instrum.* **81**, 073112 (2010).
- ¹⁶V. D. Dmitriev, S. M. Lukyanov, Y. E. Penionzhkevich, and D. K. Sattarov, *Instrum. Exp. Tech.* **25**, 283 (1982).
- ¹⁷C. Martin and S. Bowyer, *Appl. Opt.* **21**, 4206 (1982).
- ¹⁸M. Zohrabi, “Quantum control of molecular fragmentation in strong laser fields,” Ph.D. thesis (Kansas State University, 2014).
- ¹⁹H. Liu, J. Yao, and A. Puri, *Opt. Commun.* **109**, 139 (1994).
- ²⁰P. S. Banks, M. D. Feit, and M. D. Perry, *J. Opt. Soc. Am. B* **19**, 102 (2002).
- ²¹A. M. Saylor, “Measurements of ultrashort intense laser-induced fragmentation of simple molecular ions,” Ph.D. thesis (Kansas State University, 2008).

Chapter 3

Dissociation of CO^+ ions in a strong laser field

3.1 Introduction

Intense ultrashort laser pulses are becoming more essential in the physical and chemical sciences as they provide opportunities to manipulate atomic and molecular dynamics [38]. We previously studied the dissociation and ionization processes of many diatomic molecular ions, like H_2^+ [33], HD^+ [14], N_2^+ [12], O_2^+ [9, 10], CO^+ [11] and ND^+ [13], by applying a coincidence 3D momentum imaging technique. In this chapter, we present our studies on the dissociation of the CO^+ ion.

Plenty of experimental studies have been conducted on the CO molecule and its cation in a strong laser field. Kling *et al.* [11] studied the charge asymmetric dissociation of CO^+ and discussed the molecular dynamics responsible for the dependence of the branching ratio of the charge asymmetric dissociation channel on laser pulse duration. Li *et al.* [39] obtained high resolution kinetic energy release spectra for C^+ and O^+ fragments in multiphoton ionization of the CO molecule followed by dissociation of CO^+ . The authors suggested the possible pathways of dissociation from the ground doublet state $X^2\Sigma^+$ and $B^2\Sigma^+$ of CO^+ . Furthermore, in theoretical work, Okada *et al.* [40] performed multireference configuration interaction calculations of low-lying electronic states in CO^+ and provided the potential energy curves.

In studies of molecular fragmentation in a strong field, high resolution measurements of vibrational levels in an electronic state are challenging due to the involvement of a multitude of electronic states and likely dissociation pathways that could lead to the same dissociation limits. Our previous work on the dissociation of O_2^+ demonstrated the vibrational-level resolution capability of our experimental technique [9, 10].

In this work, we used a CO^+ molecular-ion beam as a target to study its dissociation in intense laser pulses produced by second harmonic generation, specifically, with a central wavelength of 393 nm and a bandwidth of 7 nm [see Figure 2.9]. The peak intensity of the laser pulse is up to 3×10^{15} W/cm² with pulse duration of 53 fs. In the experiment, a CO^+ beam with 11 keV energy is prepared in an ECR source as discussed in Chapter 2. The vibrational population of the electronic states follows the Franck-Condon distribution. The shaded region in Figure 3.1 shows the internuclear range where Franck-Condon transitions take place in the ion source.

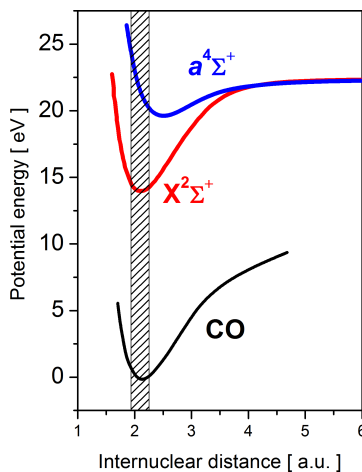


Figure 3.1: Schematic of Franck-Condon transition region from the ground electronic state of the CO molecule to electronic states of CO^+ . Potential energy curves used in this chapter are taken from reference [40].

Due to the long flight time from the ECR ion source to the interaction region (~ 18 μs), most electronic states with short life times decay [41], leaving the system mainly in the ground $X^2\Sigma^+$ state and the lowest quartet state, $a^4\Sigma^+$ [42]. The only other possible

electronic state whose population can survive until the interaction region is the $A^2\Pi$ state, which has a $3.93 \mu\text{s}$ lifetime [40]. However, only about 0.5% of measured ions from the $A^2\Pi$ state can survive and the rest will decay along the ion beam path. Our results for CO^+ dissociation suggest that at low laser intensities, e.g. $3 \times 10^{12} \text{ W/cm}^2$, dissociation of the quartet state $a^4\Sigma^+$ contributes the most. At high laser intensities, dissociation of the deep welled doublet $A^2\Pi$ state contributes too.

3.2 Dissociation of CO^+ in a strong laser field

In this work, we apply the coincidence 3D momentum imaging method that allows us to detect and separate the charged and the neutral fragments. Moreover, all measured fragmentation channels are separated from each other. In an intense laser field, we observed two dissociation channels, namely C^++O and $\text{C}+\text{O}^+$, two single ionization channels C^++O^+ and $\text{C}^{2+}+\text{O}$ as well as the double ionization channel C^++O^{2+} [see Figure 3.2(b)].

It is important to note that in this experiment we also used an electric field transverse to the ion beam supplied by a deflector to separate fragments in position [see Figure 3.2(a)]. This setup is described in detail in Bishwanath Gaire’s PhD thesis [22]. The advantage of using this setup is that it allows us to measure fragmentation channels with KER down to near 0 eV.

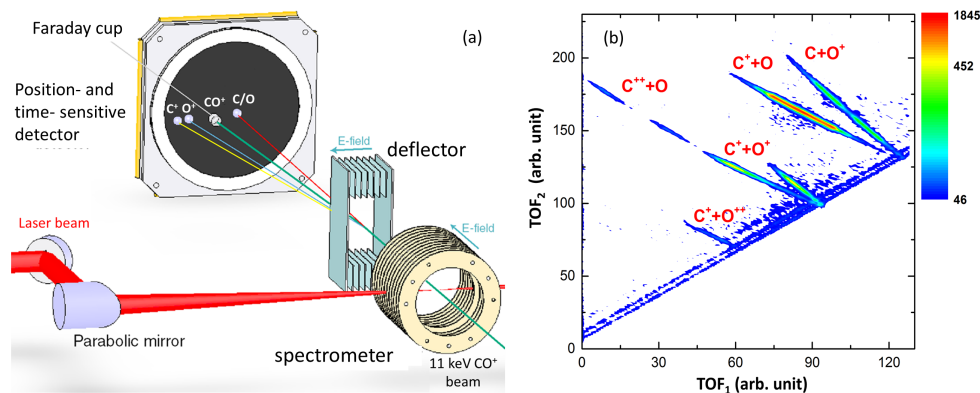


Figure 3.2: (a) Coincidence 3D momentum imaging setup with the deflector (figure adapted from [22]) and (b) coincidence TOF map for fragmentation of CO^+ induced by 53 fs linearly polarized laser pulses with 393 nm central wavelength at $3 \times 10^{15} \text{ W/cm}^2$ peak intensity.

Of the two measured dissociation channels, only the $C^+ + O$ channel will be discussed in detail in this report due to the lack of potential energy curves that lead to the $C + O^+$ channel. In the following subsections, we discuss a couple of possible dissociation pathways that contribute to the $C^+ + O$ channel. Specifically, we select a few KER peaks at low, intermediate and high laser intensities to present possible dissociation pathways.

3.2.1 Brief introduction to transition rules

In general, the peaks in the KER spectrum appearing at higher intensities may involve more photons than those appearing at lower intensities. The angular distribution of a particular KER peak informs us about the type of transition and number of photons involved in the process [9, 10]. For example, $\Sigma \rightarrow \Pi$ or $\Pi \rightarrow \Sigma$ transitions, where the projection of the total angular momentum on the molecular axis changes by $\Delta\Lambda = \pm 1$ (Λ : projection of total angular momentum on a molecular axis), are referred to as perpendicular transitions. The angular distribution of such a transition follows approximately a $\sin^{2n}\theta$ function [38], where n is the number of photons absorbed or emitted and θ is the angle between the molecular dissociation axis and the laser polarization. Similarly, $\Sigma \rightarrow \Sigma$ or $\Pi \rightarrow \Pi$ transitions, for which $\Delta\Lambda = 0$, are called parallel transitions, and their angular distribution follows a $\cos^{2n}\theta$ function [38]. The angular distributions of pathways that involve both parallel and perpendicular transitions, i.e $\Sigma \rightarrow \Pi \rightarrow \Pi$ or $\Sigma \rightarrow \Sigma \rightarrow \Pi$, follow a $\cos^{2n}\theta\sin^{2m}\theta$ function, where the n and m are, respectively, the number of photons exchanged in parallel and perpendicular transitions.

3.2.2 Low intensity - $3 \times 10^{12} \text{ W/cm}^2$

In an attempt to study the dissociation dynamics of molecular ions, it is wise to start from the lowest laser intensity that allows the molecule to dissociate [10, 20]. The reason is that, at low intensities, the number of photons involved in the dissociation is likely to be smaller than at higher intensities. The positions of the KER peaks in the spectrum allows us to trace the process and find out from what electronic state the process started. The majority

of the vibrational population of the CO^+ electronic ground state, the doublet $X^2\Sigma^+$, is at the lowest vibrational level, $v=0$. So, at a low intensity of $3 \times 10^{12} \text{ W/cm}^2$, it is less likely for the system to start from the $X^2\Sigma^+$ ($v=0$) state and overcome the deep potential well of 8.3 eV to dissociate, as it requires three 393-nm wavelength photons [see Figure 3.3(a)]. The same holds for the excited $A^2\Pi$ electronic state, where at least two photons at 393-nm are needed to overcome the potential well. However, if the system starts from the lowest quartet state, namely $a^4\Sigma^+$, then absorption of one photon at 393 nm or two photons at 786 nm leads to the dissociation of CO^+ [see Figure 3.3(b)]. In fact, our measurements provide experimental evidence that the dissociation of CO^+ into $\text{C}^+ + \text{O}$ starts from the lowest quartet state.

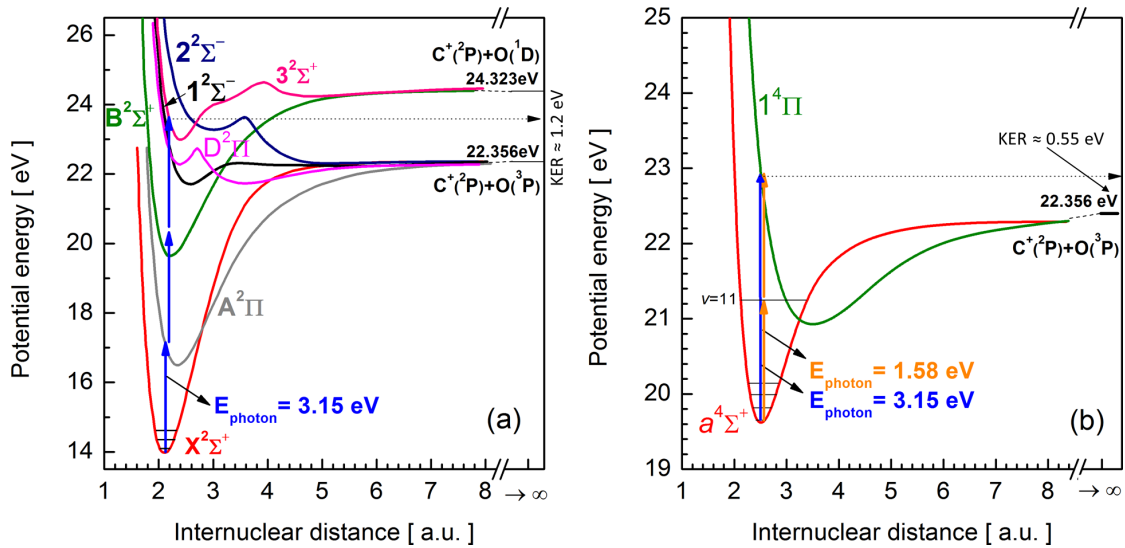


Figure 3.3: A few of the relevant potential energy curves of CO^+ for (a) doublet and (b) quartet states. Adapted from Okada *et al.* [40].

Figure 3.4 shows the KER and the KER- $\cos\theta$ distributions of the $\text{C}^+ + \text{O}$ channel at the lowest measured intensity. From the potential energy curves of the quartet states, shown in Figure 3.3(b), we estimate that the system starts from $v = 0$ of the $a^4\Sigma^+$ state and absorbs one 393-nm photon to dissociate on the $1^4\Pi$ state, releasing a kinetic energy of 0.55 eV [see peak β between the black dashed lines in Figure 3.4(a)].

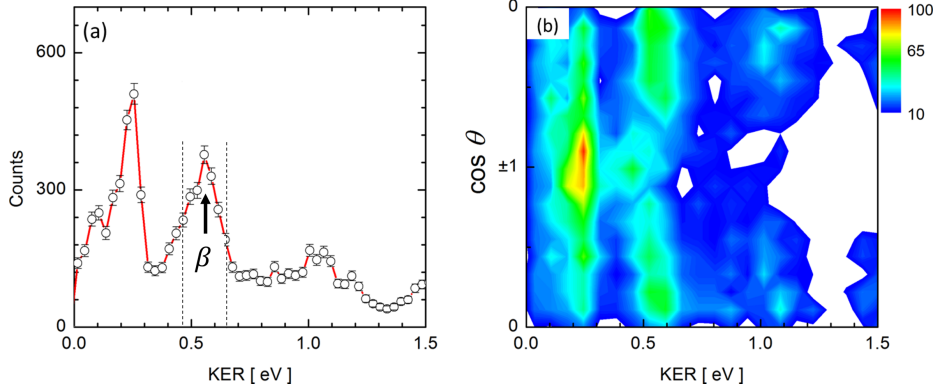


Figure 3.4: (a) The KER spectrum and (b) the KER-cos θ spectrum of the C⁺+O channel of CO⁺ dissociation in a 393 nm, 53 fs, 3×10^{12} W/cm² laser pulse.

In addition, the angular distribution corresponding to the peak at 0.55 eV in Figure 3.4(b) presents a strong component at $\cos\theta = 0$ suggesting a perpendicular transition (e.g. $\Delta\Lambda = \pm 1$). The angular distribution for events within the KER region 0.49 eV to 0.63 eV can be fit approximately with a $\sin^2\theta$ function, an indication of a one-photon perpendicular transition [see Figure 3.5].

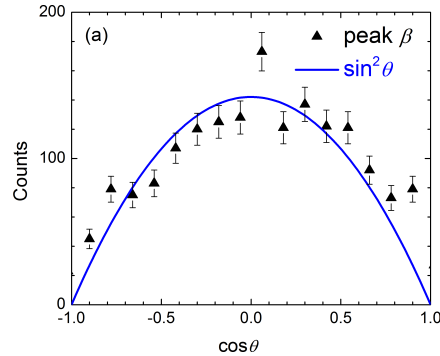


Figure 3.5: Angular distribution of peak β and a $\sin^2\theta$ fit for KER: 0.49 – 0.63 eV.

In order to further confirm the suggested pathway, we performed the experiment with a 786 nm, 30 fs laser pulse. Figure 3.6(a) shows two neighboring peaks δ and ϵ in the KER spectrum centered at 0.48 and 0.58 eV, and both peaks have perpendicular transitions according to their angular distributions [see KER-cos θ distribution in Figure 3.6(b)].

The black dashed lines in Figure 3.6(a) are the energy gates set for peaks δ and ϵ . Peak ϵ is closer in energy to the peak β , which was measured with 393 nm laser pulses. In the

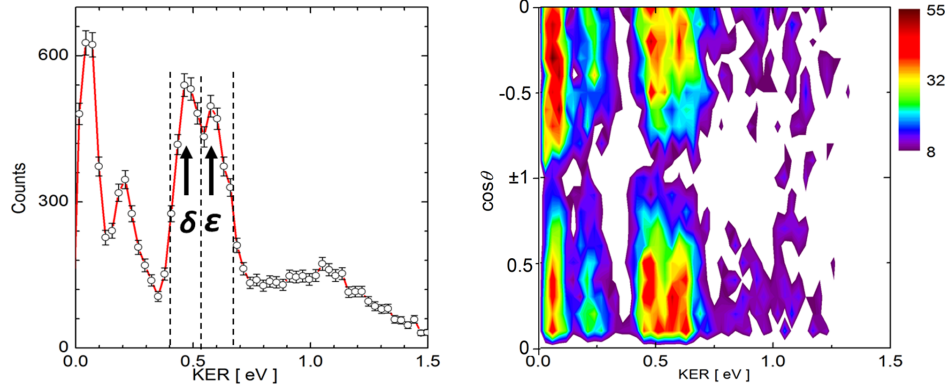


Figure 3.6: (a) The KER spectrum and (b) the KER-cos θ spectrum of the C⁺+O channel of CO⁺ dissociation in a 786 nm, 30 fs, 1×10^{13} W/cm² laser pulse.

measurement with 786 nm laser pulses, in principle, the system can undertake a two-photon transition from the $v=0$ level of the $a^4\Sigma^+$ state to the $1^4\Pi$ state [see Figure 3.3(b)]. However, with laser pulses at 786 nm wavelength, the angular distribution [see Figure 3.7(a,b)] for the KER peaks δ and ϵ conform better to a $\sin^2\theta$ function than to a $\sin^4\theta$ function, which is contradictory to the expected two-photon transition at 786 nm. This angular distribution fit, instead, indicates a one-photon perpendicular transition. A plausible scenario could be that, since the majority of the population is located toward the middle of the potential well in the $a^4\Sigma^+$ state, the system is more likely to absorb one photon of 786-nm at higher vibrational levels, e.g. $v=11$, and dissociate on the $1^4\Pi$ state. However, transition dipole moments between the $a^4\Sigma^+$ and $1^4\Pi$ states are needed to confirm the proposed transition pathways.

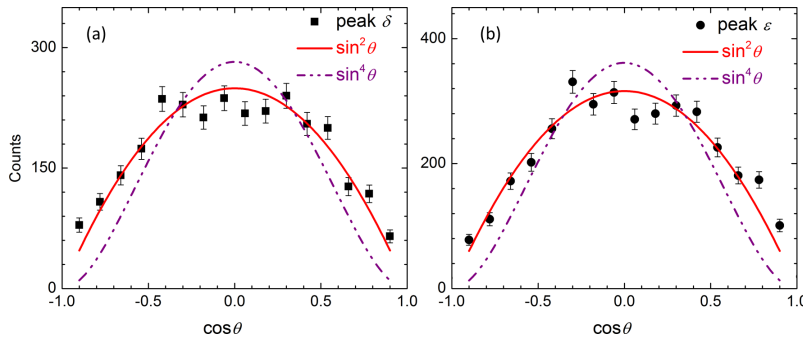


Figure 3.7: Angular distribution of (a) KER peak δ (KER: 0.43 – 0.52 eV) and (b) KER peak ϵ (KER: 0.52 – 0.65 eV) with their fit functions.

3.2.3 Intermediate intensity - $6 \times 10^{13} \text{ W/cm}^2$

In our experiment, first of all, the energy resolution was improved significantly over a previous measurement [11], which allows us to isolate and study the KER energy peak around 1.1 eV. Secondly, by measuring the $\text{C}^+ + \text{O}$ channel at low, intermediate and high laser intensities, we study the contribution of possible pathways to a peak in the KER spectrum at different intensities. At an intermediate intensity of $6 \times 10^{13} \text{ W/cm}^2$, the energy peak ϕ at around 1.1 eV presents a clear sign of a perpendicular transition [see Figure 3.8(b)].

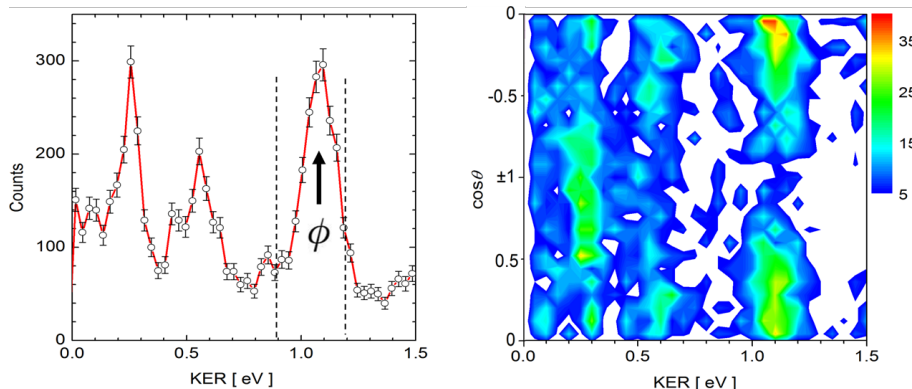


Figure 3.8: (a) The KER spectrum and (b) the KER-cos θ spectrum of the $\text{C}^+ + \text{O}$ channel of CO^+ dissociation in a 393 nm, 53 fs, $6 \times 10^{13} \text{ W/cm}^2$ laser pulse.

A further look at the angular distribution reveals that in the measurement with 393-nm laser pulses, a $\sin^2\theta$ function fits well for events within the KER peak ϕ (0.9 – 1.2 eV), indicating that a one-photon perpendicular transition can contribute to that peak [see Figure 3.9(a)]. The angular distribution in the measurement with 786-nm laser pulses, in contrast, shows that the KER peak measured around 1.1 eV has an isotropic angular distribution [see Figure 3.9(b)], suggesting an equal amount of parallel and perpendicular transitions.

According to the Franck-Condon principle, the majority of the population in the $a^4\Sigma^+$ state is located toward the middle of the well. So, it is likely for a CO^+ ion at a higher vibrational level, e.g., $v = 4$ of $a^4\Sigma^+$, to absorb one photon at 393 nm and dissociate on the $1^4\Pi$ state, releasing kinetic energy of 1.1 eV.

As to the isotropic angular distribution shown in Figure 3.9(b) for the 786-nm measurement, generally an equal contribution from a parallel and a perpendicular transition can lead to an isotropic distribution, however, more investigations need to be done to understand the possible pathways that result in such angular distribution.

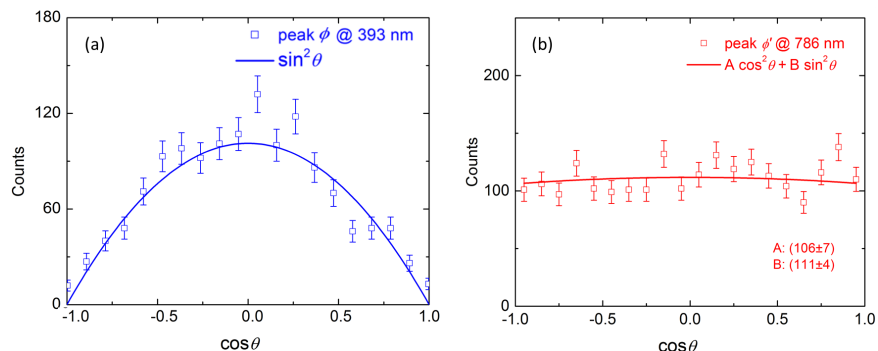


Figure 3.9: Angular distribution of (a) peak ϕ (KER: 0.9 – 1.2 eV) (blue squares) and a $\sin^2\theta$ fit (blue line) in a 393 nm, 53 fs, 6×10^{13} W/cm² laser pulse and (b) the equivalent KER peak ϕ' in a 786 nm, 30 fs, 8×10^{13} W/cm² laser pulse (red squares) and a fit to a constant (red line).

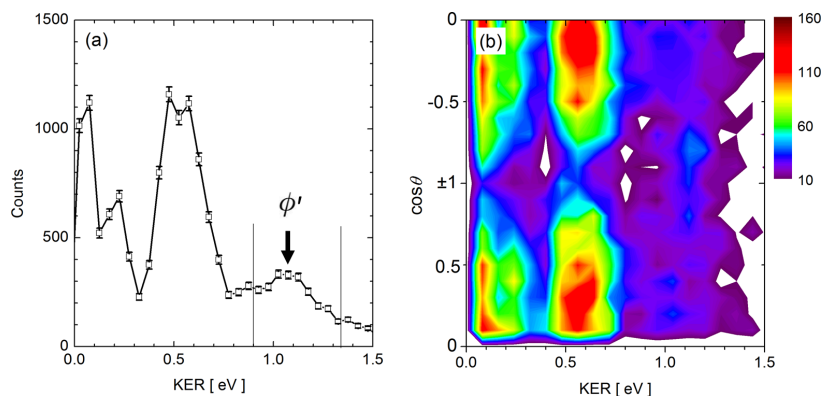


Figure 3.10: (a) The KER spectrum and (b) the KER- $\cos\theta$ spectrum of the C⁺+O channel of CO⁺ dissociation in a 786 nm, 30 fs, 8×10^{13} W/cm² laser pulse.

Figure 3.10 shows the KER and KER- $\cos\theta$ distributions of the C⁺+O channel with laser pulses at 786 nm, 30 fs and 8×10^{13} W/cm². At similar intermediate laser intensities, the KER peak at 1.1 eV is significantly smaller than the peak at 0.55 eV in the 786-nm measurement as compared to the 393-nm measurement. Due to the limited availability of potential energy curves as well as transition dipole moments between the relevant electronic

states, nailing down the exact pathway remains a challenge. However, the plausible pathways proposed in this section can be further confirmed if this information becomes available in the future.

At both low and intermediate intensities, we chose initial vibrational levels of the $a^4\Sigma^+$ state by matching KER peak values. Although the angular distribution of the energy peaks are consistent with the type of transition and the number of photons involved, without proper attention to the Franck-Condon population of different vibrational states as well as the transition probabilities from vibrational levels of the $a^4\Sigma^+$ to the $1^4\Pi$ state, our pathway confirmation is questionable. Figure 3.11 shows the transition probabilities from vibrational levels in $a^4\Sigma^+$ to the $1^4\Pi$ state. The transition dipole moments between the two states are missing in the current literature, but in our experience transition dipole moments usually are not strongly dependent on the internuclear distance in the molecule. So, in the results shown in Figure 3.11, the transition dipole moment was considered to be a constant. **FC** is the Franck-Condon population of a vibrational state of $a^4\Sigma^+$, $\Psi_{a^4\Sigma^+}(v)$ and $\Psi_{1^4\Pi}(E)$ are respectively the bound state wave function for a vibrational level v of the $a^4\Sigma^+$ state and the continuum state wave function on the $1^4\Pi$ state.

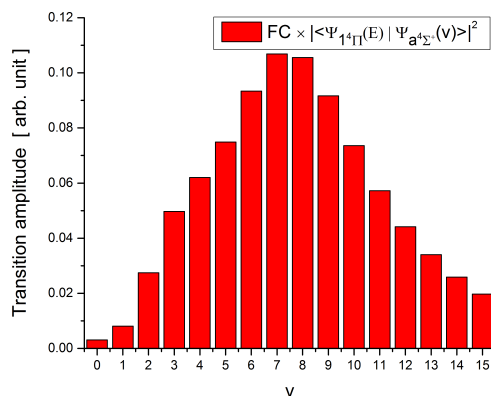


Figure 3.11: The expected yield of dissociation from vibrational levels of the $a^4\Sigma^+$ state to the $1^4\Pi$ state after absorbing one 393-nm photon.

One can clearly see that the calculation result shown in Figure 3.11 is not consistent with our interpretation of the peaks at the low and the intermediate intensities. In order

to nail down the two specific pathways proposed in Section 3.2.3 and 3.2.4, more potential energy curves as well as the transition dipole moments among relevant states are needed.

3.2.4 High intensity - $3 \times 10^{15} \text{ W/cm}^2$

At high intensities, more photons are likely to be absorbed from the laser field, and the dissociation of CO^+ can be initiated from the lower electronic states with deep potential wells, such as the $X^2\Sigma^+$ and $A^2\Pi$ states. However, due to the opening of many possible pathways as the result of increased intensity, tracing a particular process becomes more difficult. Figure 3.12 presents the KER and KER- $\cos\theta$ distributions of the $\text{C}^+ + \text{O}$ channel at the peak laser intensity of $3 \times 10^{15} \text{ W/cm}^2$. According to Figure 3.12(a), a peak at 1.2 eV dominates the KER spectrum (labeled as χ), and the angular distribution shown in panel (b) suggests that this dominant peak has a large parallel transition component and a smaller perpendicular component.

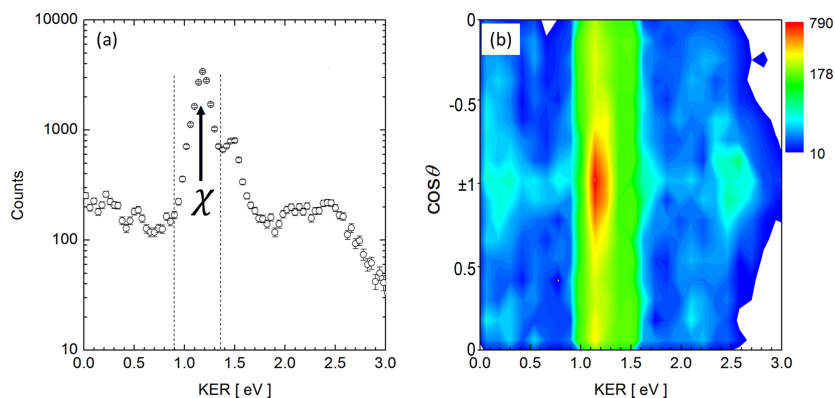


Figure 3.12: (a) The KER spectrum and (b) the KER- $\cos\theta$ spectrum of the $\text{C}^+ + \text{O}$ channel of CO^+ dissociation in a 393 nm, 53 fs, $3 \times 10^{15} \text{ W/cm}^2$ laser pulse.

In the previous subsection, we discussed the energy peak ϕ ($\text{KER} \approx 1.1 \text{ eV}$) at intermediate intensities and suggested that it is due to a perpendicular transition. At higher intensities, another pathway contributes in this KER region. Figure 3.13 shows the KER- $\cos\theta$ distributions at various intensities, and from it we can see that the dominant KER feature that appears at $3 \times 10^{15} \text{ W/cm}^2$ is very sensitive to intensity. So, the number

of photons involved in the process is likely to be more than one. This will exclude the quartet states, because absorbing more than one photon leads to high KER values, e.g., $a^4\Sigma^+ + 2\omega \rightarrow 1^4\Pi$ yields 3.65 eV.

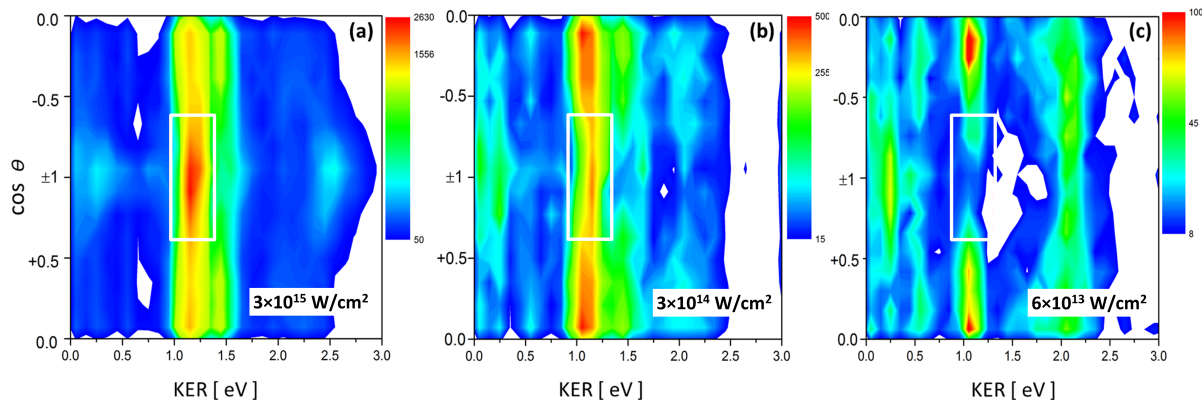


Figure 3.13: KER- $\cos\theta$ distribution of C^+O channel in (a) 3×10^{15} W/cm²; (b) 3×10^{14} W/cm²; (c) 6×10^{13} W/cm² laser pulse having a duration of 53 fs and a central wavelength of 393 nm.

In contrast, the CO^+ can start from the $X^2\Sigma^+$ ground vibrational level, absorb a few photons and dissociate with the measured KER. However, the angular distribution of the final KER peak must be consistent with the type of transition as well as the number of photons exchanged. In this specific case, the angular distribution of the dominant peak at 1.2 eV indicates a strong parallel transition. This will exclude any type of direct transition starting from the $X^2\Sigma^+$ ground doublet state, because the only possible parallel transition lands on the highly excited $3^2\Sigma^+$ state and results in a KER of 2.6 eV. Figure 3.14(b) shows the angular distribution of events in the KER peak χ (KER: 0.9 – 1.34 eV), and the highly aligned component at $\cos\theta = \pm 1$ is approximately fit by a $\cos^4\theta$ function, suggesting a two-photon parallel transition. The $\sin^2\theta$ component is most likely due to the transitions described in Section 3.2.3 for intermediate intensities.

Although only 0.5% of the ions from the doublet $A^2\Pi$ state will survive to the interaction region, as mentioned in Section 3.1, a possible transition starting from this state can not be excluded. In particular, a two 393-nm photon absorption in a parallel transition starting from the lower vibrational levels of the $A^2\Pi$ state to the $D^2\Pi$ state will result in a KER

of 1.2 eV, and has the measured $\cos^4\theta$ distribution, making it the most likely pathway for KER peak χ [see Figure 3.14(a)].

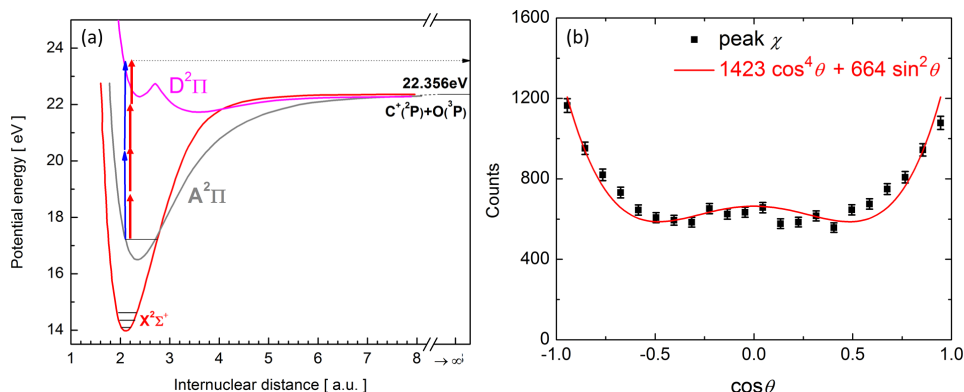


Figure 3.14: (a) Schematic of transitions for $A^2\Pi + 2\omega \rightarrow D^2\Pi$. Blue arrow is equivalent to a 393-nm photon and the red arrow represents the 786-nm photons. Potential energy curves in this figure are taken from reference [40]. (b) Angular distribution of KER peak χ (KER: 0.9 – 1.34 eV). The laser pulse duration is 53 fs and the central wavelength is 393 nm with a 3×10^{15} W/cm² peak intensity.

For the 786-nm measurement, the peak corresponding to peak χ is labeled peak γ in Figure 3.15(a). Once again, we choose events within the KER region 0.9 - 1.34 eV [the black dashed lines in Figure 3.15(a)]. Figure 3.16 shows the angular distribution for events within that region. The fit function to the measured data consists of a $\cos^8\theta$ and a constant term. The cosine term indicates a parallel transition with an exchange of four photons at 786 nm, e.g. $A^2\Pi + 4\omega \rightarrow D^2\Pi$. This result is consistent with the two 393-nm photons transition shown in Figure 3.14(a). The isotropic term in the fit function is consistent with the isotropic contribution from an intermediate intensity in 786 nm laser field as described in Section 3.2.3 and a likely scenario for this isotropic distribution may come from two independent one-photon transitions, namely a perpendicular and parallel transition.

The experiment with a high intensity 786 nm laser pulses reveals a different KER spectrum than that measured with 393 nm [see Figure 3.15(a)]. At an intensity of 2.8×10^{15} W/cm², the structure in the KER spectrum is washed out compared to the measurements with 393 nm laser pulses. The reason may be due to the significant differences in bandwidths

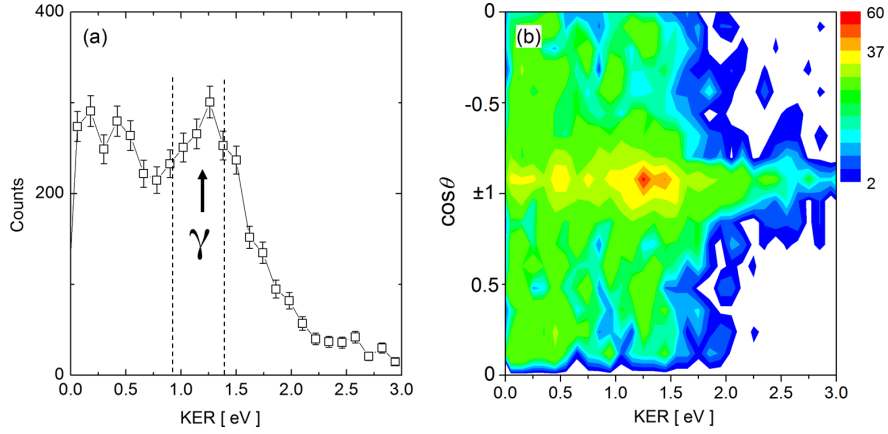


Figure 3.15: (a) The KER spectrum and (b) the KER-cos θ spectrum of the C⁺+O channel of CO⁺ dissociation in a 786 nm, 30 fs, 2.8×10^{15} W/cm² laser pulse.

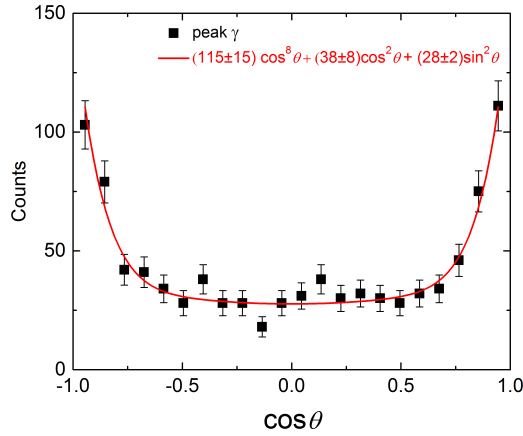


Figure 3.16: The angular distribution fit for events in peak γ , e.g. KER: 0.9 – 1.34 eV in a 786 nm, 30 fs, 2.8×10^{15} W/cm² laser pulse.

of the two laser pulses, specifically 30 nm and 7 nm in the 786-nm and 393-nm measurements, respectively [see Table 2.1]. The KER-cos θ distribution shown in Figure 3.15(b) suggests a parallel transition for a broad KER region from 0 to 3 eV.

Tackling the problem of finding dissociation pathways is a difficult and time consuming task. To nail a transition pathway requires sufficient experimental and theoretical information. In our measurements, conducted at two laser wavelengths, namely 393 nm and 786 nm, we obtained high quality data with rich KER structures. Furthermore, we proposed plausible pathways at low, intermediate and high laser intensities for a few peaks in the KER spectra. However, to further confirm the proposed pathways, one needs to obtain

accurate transition dipole moments as well as the potential energy curves. In particular, obtaining potential energy curves that lead to the $C+O^+$ channel would open the door to study the dissociation of CO^+ into both channels. In addition, one can extend the measurements by changing the laser pulse duration, e.g. (1) use 5 fs pulses at 786 nm produced in a hollow-core fiber, and (2) use transform limited 393 nm laser pulses. These additional measurements may provide more information on the dissociation dynamics.

Chapter 4

Three-body fragmentation of CO_2^+ into $\text{C}^+ + \text{O}^+ + \text{O}^+$ in a strong laser field

4.1 Introduction

Carbon dioxide, CO_2 , is a linear triatomic molecule that is important in our atmosphere as a product of photochemical processes [43] as well as playing an essential role in the carbon cycle [44]. In both the laser and collisions fields, numerous experimental and theoretical works have been conducted to study this molecule. In this chapter, we focus on the fragmentation of CO_2^+ into $\text{C}^+ + \text{O}^+ + \text{O}^+$.

In strong field studies, Hishikawa *et al.* [45] used 100 fs laser pulses at 795 nm and measured the fragmentation of CO_2 molecules. They claimed that the structural deformation of the molecule is caused by the strong laser field based on the measurements of the $\text{C}^+ + \text{O}^+ + \text{O}^+$ channel. In order to confirm that claim, Sato *et al.* [46] calculated the potential energy surfaces of neutral, cation and dication CO_2 and concluded that the observed structural deformation of the CO_2^{3+} is due to the bending motion during the propagation on a CO_2^{2+} surface before the system absorbs more energy to reach the repulsive CO_2^{3+} surface. The propagation on a CO_2^{2+} surface was reported to be on a 90 fs time scale. However, recently, Bocharova *et al.* [47] and Wu *et al.* [48] studied the channel with shorter laser pulses. Bocharova *et al.* [47] used laser pulses with various pulse durations from 7 to 200 fs

at a laser intensity of 10^{14} W/cm² and observed that the KER of the C⁺+O⁺+O⁺ channel always peaks at 21 eV. Wu *et al.* [48] used a 24 fs pulse at 1×10^{15} W/cm² and claimed that the geometrical structure of CO₂³⁺ is very close to linear, i.e. the structure of the CO₂ molecule before laser irradiation. Furthermore, Wu *et al.* [48] claimed to distinguish the sequential breakup process in the C⁺+O⁺+O⁺ channel, where a CO₂³⁺ ion breaks into CO²⁺+O⁺ followed by unimolecular dissociation of the rotating metastable CO²⁺, from the nonsequential process, where all fragments in the C⁺+O⁺+O⁺ channel break up simultaneously. Wu *et al.* [48] used the energy correlation between the two O⁺ fragments in the C⁺+O⁺+O⁺ channel, see Figure 4.1(a), to separate the nonsequential (outside red line) and sequential breakup (within red line) events. Panels (b) and (c) show the Newton diagrams of nonsequential and sequential breakup events, respectively. In panel (c), the area within the circular red-dashed lines presents proof of the rotating intermediate CO²⁺.

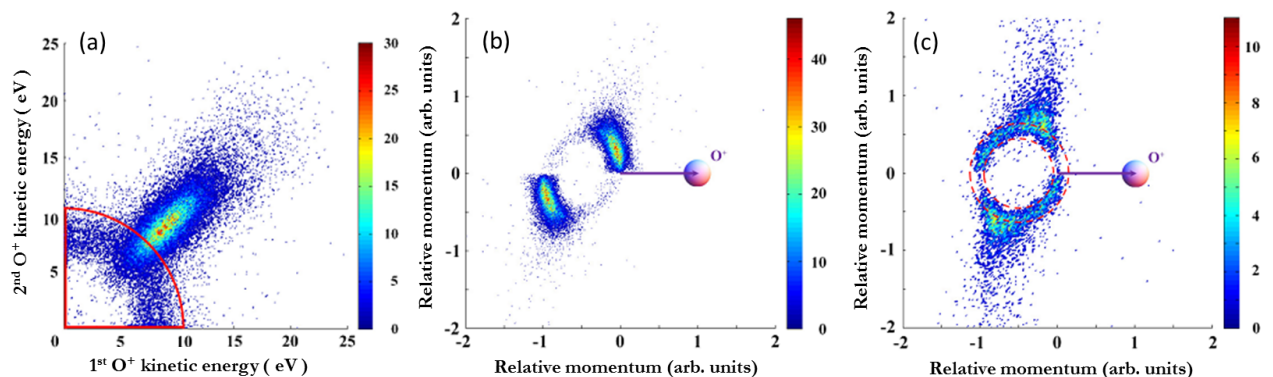


Figure 4.1: (a) Correlation between the two O⁺ energies in the C⁺+O⁺+O⁺ channel. (b) Newton diagrams of the C⁺+O⁺+O⁺ channel for nonsequential events and (c) for sequential events. The reported laser profile: 800 nm, 24 fs linearly polarized laser field at an intensity of 1×10^{15} W/cm². Adapted from reference [48].

In collision studies of the CO₂ molecule, Neumann *et al.* [49] conducted measurements on the fragmentation of CO₂³⁺ after multiple electron capture from a CO₂ molecule by a 3.2 KeV/u Ar⁸⁺ ion. They claimed that the fragmentation of CO₂³⁺ contains sequential and direct as well as asynchronous processes, where the bonds of the molecular ion break when the geometry of the molecule is asymmetric.

In this chapter, we discuss our investigations of three-body breakup of CO_2^+ ions into $\text{C}^+ + \text{O}^+ + \text{O}^+$ in intense femtosecond laser pulses. Specifically, we focus on symmetric and asymmetric breakup of the CO_2^{3+} ion. Initially, a CO_2^+ ion beam target is ionized by a linearly polarized 26 fs intense laser pulse centered at a wavelength of 786 nm with a peak intensity of $6.5 \times 10^{15} \text{ W/cm}^2$. Using the coincidence 3D momentum imaging technique, all the measured two- and three-body fragmentation channels were identified [see Figure 4.2].

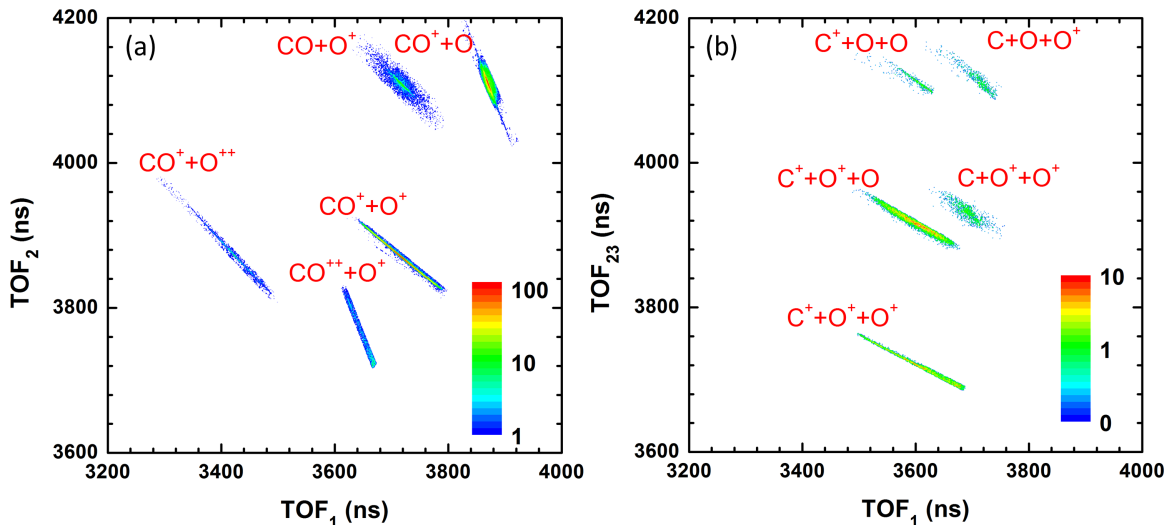


Figure 4.2: Coincidence TOF map for (a) two- and (b) three-body fragmentation of CO_2^+ induced by 26 fs linearly polarized laser pulses with a peak intensity of $6.5 \times 10^{15} \text{ W/cm}^2$; Note: in panel (a) individual two-body channels are gated on the CM momentum, and in (b) each three-body channel is gated on the TOF (see 2.11) in order to separate real events from random coincidences.

As opposed to most studies that used neutral CO_2 as an initial target [45, 47–49], we used a CO_2^+ ion beam target to study the fragmentation. Our results show that the fragmentation of CO_2^{3+} involves symmetric and asymmetric breakup. In symmetric breakup, two O^+ fragment momenta in the molecular frame are similar in size, while in asymmetric breakup, one O^+ obtains much larger momentum compared to the other O^+ . Furthermore, we introduce a new method to separate the symmetric breakup events from asymmetric breakup.

4.2 Symmetric and asymmetric breakup of CO_2^+ into $\text{C}^+ + \text{O}^+ + \text{O}^+$

Using the experimental method described in Chapter 2, three-dimensional momentum vectors of the fragments in the $\text{C}^+ + \text{O}^+ + \text{O}^+$ channel, namely \mathbf{P}_{C^+} , $\mathbf{P}_{\text{O}_{(1)}^+}$ and $\mathbf{P}_{\text{O}_{(2)}^+}$, are evaluated. Two distinct breakup mechanisms can be introduced to understand the dissociation of the CO_2^{3+} ion, namely symmetric and asymmetric breakup of the $\text{C}^+ + \text{O}^+ + \text{O}^+$ channel.

In symmetric breakup, both C-O bonds stretch equally, while in asymmetric breakup, one C-O bond stretches more than the other. In order to distinguish these two scenarios, we use the measured momentum vectors of the three fragments, shown in Figure 4.3, and define two new momentum vectors, namely \mathbf{P}_{sum} and \mathbf{P}_{diff} , as

$$\mathbf{P}_{\text{sum}} = \mathbf{P}_{\text{O}_{(1)}^+} + \mathbf{P}_{\text{O}_{(2)}^+} \quad (4.1)$$

$$\mathbf{P}_{\text{diff}} = \mathbf{P}_{\text{O}_{(1)}^+} - \mathbf{P}_{\text{O}_{(2)}^+}. \quad (4.2)$$

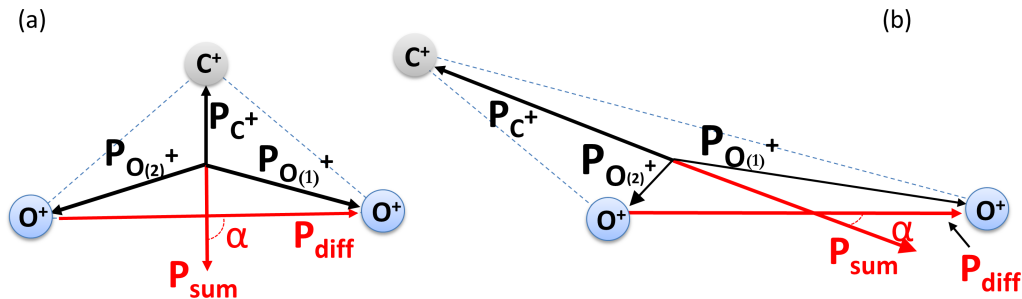


Figure 4.3: (a) Symmetric breakup for which $|\mathbf{P}_{\text{O}_{(1)}^+}| \approx |\mathbf{P}_{\text{O}_{(2)}^+}|$ and (b) asymmetric breakup, for which $|\mathbf{P}_{\text{O}_{(1)}^+}| \gg |\mathbf{P}_{\text{O}_{(2)}^+}|$ (the choice of 1st and 2nd for the O^+ fragments is arbitrary).

In Figure 4.3, the momentum vectors are in the molecular frame where,

$$\mathbf{P}_{\text{C}^+} + \mathbf{P}_{\text{O}_{(1)}^+} + \mathbf{P}_{\text{O}_{(2)}^+} = 0 \quad (4.3)$$

due to conservation of momentum.

Using the angle between momentum vectors \mathbf{P}_{sum} and \mathbf{P}_{diff} , α , shown in Figure 4.3, we define symmetric breakup events as those with α close to $\pi/2$, while asymmetric breakup

events are the ones for which α is far from $\pi/2$. The expression for $\cos\alpha$ is

$$\cos\alpha = \frac{\mathbf{P}_{\text{sum}} \cdot \mathbf{P}_{\text{diff}}}{|\mathbf{P}_{\text{sum}}||\mathbf{P}_{\text{diff}}|}. \quad (4.4)$$

Figure 4.4 presents the $\cos\alpha$ distribution for all events, and the dominant breakup happens when $\alpha = \pi/2$. Figure 4.5 presents an example of separating the symmetric and asymmetric breakup events by setting gates on the angular distribution of $\cos\alpha$.

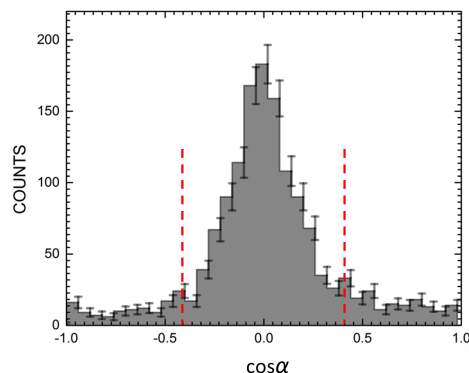


Figure 4.4: The number of $C^+ + O^+ + O^+$ breakup events as a function of $\cos\alpha$. Symmetric breakup: events within the two red dashed lines. Asymmetric breakup: events outside the red dashed lines. (preliminary results).

Figure 4.5(a) shows the Dalitz plot for all $C^+ + O^+ + O^+$ events. By extracting events within and outside of the gates set on Figure 4.4 (red dashed lines), we get symmetric and asymmetric breakup events in panel (b) and (c), respectively.

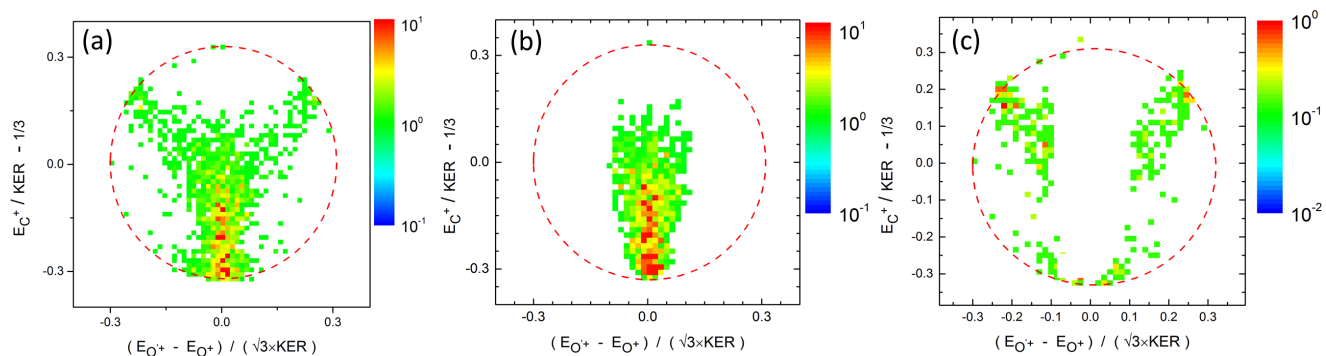


Figure 4.5: Dalitz plot of the $C^+ + O^+ + O^+$ channel: (a) all events, (b) symmetric breakup: $|\cos\alpha| < 0.4$, and (c) asymmetric breakup: $|\cos\alpha| > 0.4$.

Using the Dalitz plots generated after setting $\cos\alpha$ gates for symmetric and asymmetric breakup events, we can study, e.g., the kinetic energy of the C^+ fragment with respect to the total KER by projecting Figure 4.5(b) onto its vertical axis [see Figure 4.6].

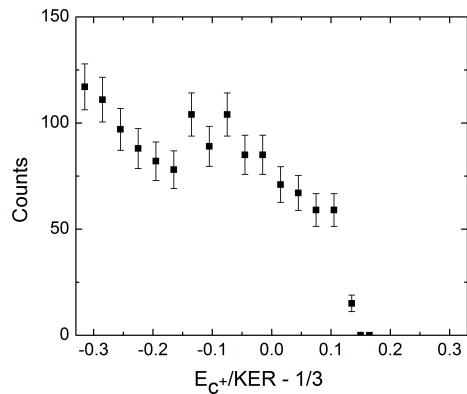


Figure 4.6: The yield of C^+ fragments as a function of the relative energy with respect to the total KER of the $C^+ + O^+ + O^+$ channel undergoing symmetric breakup.

One can see from Figure 4.6 that the three-body breakup happens predominantly when $E_{C^+} \approx 0$ and the yield decreases discontinuously when the energy of C^+ relative to the total KER of the $C^+ + O^+ + O^+$ channel increases. Although further investigation is needed to understand this phenomenon, this example shows that the method of using $\cos\alpha$ gates to separate symmetric and asymmetric channels can be useful to provide further information on the three-body breakup dynamics of $C^+ + O^+ + O^+$.

Chapter 5

Summary and outlook

To summarize, in this master's report we used a coincidence 3D momentum imaging technique to study the interactions of femtosecond laser pulses with molecular ion beams, specifically, CO^+ and CO_2^+ . The main goal in our studies is to understand the underlying fragmentation dynamics of ionic targets.

In the study of the dissociation of CO^+ in intense ultrafast femtosecond laser pulses, we discovered that at low laser intensities ($3 \times 10^{12} \text{ W/cm}^2$), dissociation of the system most likely starts from the quartet state $a^4\Sigma^+$ and ends on the $1^4\Pi$ electronic state. The absorption of one photon at 393 nm or 786 nm from a few specific vibrational states matches some peaks in the measured KER spectrum. However, it is unclear why other vibrational states do not contribute. Further structure information is needed to resolve this issue. When the laser intensity is increased to $3 \times 10^{15} \text{ W/cm}^2$, the system can absorb more photons, thus the doublet electronic state $A^2\Pi$, which has a deep potential well, contributes to the dissociation process. The KER spectrum measured for the $\text{C}^+\text{+O}$ channel at high laser intensities is the convolution of processes contributed from low, medium and high laser intensities because of intensity averaging.

We also studied the three-body breakup of CO_2^+ into $\text{C}^+\text{+O}^+\text{+O}^+$, and preliminary results are presented. The analysis method of three-body fragmentation channels is described, and a method to separate symmetric and asymmetric breakup events is introduced. Specifically, we use the angle between P_{sum} and P_{diff} momentum vectors to distinguish between

these two breakup scenarios.

In addition, we introduced a reflective telescope setup to achieve higher intensity UV laser pulses as a technical improvement of our experimental method. By implementing this reflective telescope, the conversion rate of UV light generation through a BBO crystal is increased by a factor of about 1.5. Moreover, a higher laser intensity of 3×10^{15} W/cm² is reached at the central wavelength of 393 nm with a bandwidth of 7 nm.

In addition, we studied the position dependence of timing signals picked off of a MCP detector. We discovered a wide time spread of 280 ps through the entire surface of our MCP detector. This study and its findings are described in a publication from our group, which is embedded at the end of Chapter 2.

In both the study of CO⁺ dissociation and three-body fragmentation of CO₂⁺, there is plenty of future work that can be conducted in order to better understand their fragmentation mechanisms. For CO⁺, by obtaining more complete structure calculations which include dipole transition moments between essential electronic states, one can extend the study and find possible pathways for KER peaks that are unknown. Furthermore, the other dissociation channel C+O⁺ can also be studied once the relevant potential energy curves, which are lacking in the current literature, are computed. In the study of three-body fragmentation of CO₂⁺, using laser pulses with higher repetition rates, e.g PULSAR at 10 kHz, can provide greatly improved statistics, thus opening the door to explore three-body breakup channels with low dissociation rates, e.g. C⁺+O+O.

Bibliography

- [1] U. Ablikim, M. Zohrabi, Bethany Jochim, B. Berry, T. Severt, K. D. Carnes, and I. Ben-Itzhak, Note: Position dependence of time signals picked off a microchannel plate detector, *Rev. Sci. Instrum.* **86**, 016111 (2015).
- [2] A. H. Zewail, Femtochemistry: atomic-Scale dynamics of the chemical bond, *J. Phys. Chem. A* **104**, 5660 (2000).
- [3] C. Guo, M. Li, J. Nibarger, and G. Gibson, Single and double ionization of diatomic molecules in strong laser fields, *Phys. Rev. A* **58**, R4271 (1998).
- [4] D. Pavičić, A. Kiess, T. W. Hänsch, and H. Figger, Intense-laser-field ionization of the hydrogen molecular ions H_2^+ and D_2^+ at critical internuclear distances, *Phys. Rev. Lett.* **94**, 163002 (2005).
- [5] Itzik Ben-Itzhak, Pengqian Wang, Jiangfan Xia, A. Max Sayler, Mark A. Smith, J. W. Maseberg, Kevin D. Carnes, and Brett D. Esry, Dissociation and ionization of molecular ions by ultra-short intense laser pulses probed by coincidence 3D momentum imaging, *Nucl. Instrum. Methods Phys. Res. B* **233**, 56 (2005).
- [6] I. Ben-Itzhak, P. Q. Wang, J. F. Xia, A. M. Sayler, M. A. Smith, K. D. Carnes, and B. D. Esry, Dissociation and ionization of H_2^+ by ultrashort intense laser pulses probed by coincidence 3D momentum imaging, *Phys. Rev. Lett.* **95**, 073002 (2005).
- [7] S. Voss, A. S. Alnaser, X-M Tong, C. Maharjan, P. Ranitovic, B. Ulrich, B. Shan, Z. Chang, C. D. Lin, and C. L. Cocke, High resolution kinetic energy release spectra and angular distributions from double ionization of nitrogen and oxygen by short laser pulses, *J. Phys. B: At. Mol. Opt. Phys.* **37**, 4239 (2004).

- [8] W. Guo, J. Zhu, B. Wang, Y. Wang, and L. Wang, Angular distributions of fragment ions of N_2 in a femtosecond laser field, *Phys. Rev. A* **77**, 033415 (2008).
- [9] M. Zohrabi, J. McKenna, B. Gaire, N. G. Johnson, K. D. Carnes, S. De, I. A. Bocharova, M. Magrakvelidze, D. Ray, I. V. Litvinyuk, C. L. Cocke, and I. Ben-Itzhak, Vibrationally resolved structure in O_2^+ dissociation induced by intense ultrashort laser pulses, *Phys. Rev. A* **83**, 053405 (2011).
- [10] A. M. Sayler, P. Q. Wang, K. D. Carnes, B. D. Esry, and I. Ben-Itzhak, Determining laser-induced dissociation pathways of multielectron diatomic molecules: Application to the dissociation of O_2^+ by high-intensity ultrashort pulses, *Phys. Rev. A* **75**, 063420 (2007).
- [11] N. G. Kling, J. McKenna, A. M. Sayler, B. Gaire, M. Zohrabi, U. Ablikim, K. D. Carnes, and I. Ben-Itzhak, Charge asymmetric dissociation of a CO^+ molecular-ion beam induced by strong laser fields, *Phys. Rev. A* **87**, 013418 (2013).
- [12] B. Gaire, J. McKenna, A. M. Sayler, N. G. Johnson, E. Parke, K. D. Carnes, B. D. Esry, and I. Ben-Itzhak, High kinetic energy release upon dissociation and ionization of an N_2^+ beam by intense few-cycle laser pulses, *Phys. Rev. A* **78**, 033430 (2008).
- [13] J. McKenna, A. M. Sayler, B. Gaire, N. G. Johnson, E. Parke, K. D. Carnes, B. D. Esry, and I. Ben-Itzhak, Intensity dependence in the dissociation branching ratio of ND^+ using intense femtosecond laser pulses, *Phys. Rev. A* **77**, 063422 (2008).
- [14] J. McKenna, A. M. Sayler, B. Gaire, N. G. Johnson, M. Zohrabi, K. D. Carnes, B. D. Esry, and I. Ben-Itzhak, Permanent dipole transitions remain elusive in HD^+ strong-field dissociation, *J. Phys. B: At. Mol. Opt. Phys.* **42**, 121003 (2009).
- [15] A. M. Sayler, J. McKenna, B. Gaire, N. G. Kling, K. D. Carnes, B. D. Esry, and I. Ben-Itzhak, Elucidating isotopic effects in intense ultrafast laser-driven D_2H^+ fragmentation, *J. Phys. B: At. Mol. Opt. Phys.* **47**, 031001 (2014).

- [16] J. McKenna, A. M. Sayler, B. Gaire, N. G. Kling, B. D. Esry, K. D. Carnes, and I. Ben-Itzhak, Frustrated tunnelling ionization during strong-field fragmentation of D_3^+ , *New J. Phys.* **14**, 103029 (2012).
- [17] A. M. Sayler, J. McKenna, B. Gaire, N. G. Kling, K. D. Carnes, and I. Ben-Itzhak, Measurements of intense ultrafast laser-driven D_3^+ fragmentation dynamics, *Phys. Rev. A* **86**, 033425 (2012).
- [18] B. Gaire, J. McKenna, M. Zohrabi, K. D. Carnes, B. D. Esry, and I. Ben-Itzhak, Dynamics of D_3^+ slow dissociation induced by intense ultrashort laser pulses, *Phys. Rev. A* **85**, 023419 (2012).
- [19] B. Gaire, J. McKenna, N. G. Johnson, A. M. Sayler, E. Parke, K. D. Carnes, and I. Ben-Itzhak, Laser-induced multiple ionization of molecular ion beams: N_2^+ , CO^+ , NO^+ , and O_2^+ , *Phys. Rev. A* **79**, 063414 (2009).
- [20] A. M. Sayler, *Measurements of ultrashort intense laser-induced fragmentation of simple molecular ions*, PhD thesis, Kansas State University, 2008.
- [21] M. Zohrabi, *Quantum control of molecular fragmentation in strong laser fields*, PhD thesis, Kansas State University, 2014.
- [22] B. Gaire, *Imaging of slow dissociation of the laser induced fragmentation of molecular ions*, PhD thesis, Kansas State University, 2011.
- [23] N. G. Kling, *Controlling the dynamics of electrons and nuclei in ultrafast strong laser fields*, PhD thesis, Kansas State University, 2013.
- [24] A. S. Coolidge, H. M. James, and R. D. Present, A study of the Franck-Condon principle, *J. Chem. Phys.* **4**, 193 (1936).
- [25] Z. Amitay, A. Baer, M. Dahan, J. Levin, Z. Vager, D. Zajfman, L. Knoll, M. Lange, D. Schwalm, R. Wester, A. Wolf, I. F. Schneider, and A. Suzor-Weiner, Dissociative

- recombination of vibrationally excited HD^+ : State-selective experimental investigation, *Phys. Rev. A* **60**, 3769 (1999).
- [26] R. Trebino and D. J. Kane, Using phase retrieval to measure the intensity and phase of ultrashort pulses: frequency-resolved optical gating, *J. Opt. Soc. Am. A* **10**, 1101 (1993).
- [27] R. Trebino, K. W. Delong, D. N. Fittinghoff, J. N. Sweetser, M. A. Krumbugel, B. A. Richman, and D. J. Kane, Measuring ultrashort laser pulses in the time-frequency domain using frequency-resolved optical gating, *Rev. Sci. Instrum.* **68**, 3277 (1997).
- [28] RoentDek Handels GmbH, <http://www.roentdek.com/>.
- [29] Robert W. Boyd, *Nonlinear Optics, Third Edition*, (Academic Press, San Diego 2008).
- [30] Valentin G. Dmitriev, Gagik G. Gurzadyan, David N. Nikogosyan, *Handbook of Non-linear Optical Crystals*, (Springer-Verlag Berlin Heidelberg, New York 1999).
- [31] P. Hello and C. N. Man, Design of a low-loss off-axis beam expander, *Appl. Opt.* **35**, 2534 (1996).
- [32] J. McKenna, A. M. Sayler, F. Anis, N. G. Johnson, B. Gaire, U. Lev, M. A. Zohrabi, K. D. Carnes, B. D. Esry, and I. Ben-Itzhak, Vibrationally cold CO^{2+} in intense ultrashort laser pulses, *Phys. Rev. A* **81**, R061401 (2010).
- [33] J. McKenna, A. M. Sayler, F. Anis, B. Gaire, N. G. Johnson, E. Parke, J. J. Hua, H. Mashiko, C. M. Nakamura, E. Moon, Z. Chang, K. D. Carnes, B. D. Esry, and I. Ben-Itzhak, Enhancing high-order above-threshold dissociation of H_2^+ beams with few-cycle laser pulses, *Phys. Rev. Lett.* **100**, 133001 (2008).
- [34] P. Q. Wang, A. M. Sayler, K. D. Carnes, J. F. Xia, M. A. Smith, B. D. Esry, and I. Ben-Itzhak, Dissociation of H_2^+ in intense femtosecond laser fields studied by coincidence three-dimensional momentum imaging, *Phys. Rev. A* **74**, 043411 (2006).

- [35] Qi Zhang, Kun Zhao, Zenghu Chang, Determining time resolution of microchannel plate detectors for electron time-of-flight spectrometers, *Rev. Sci. Instrum.* **81**, 073112 (2010).
- [36] J. Va'vra, J. Benitez, D.W.G.S. Leith, G. Mazaheri, B. Ratcliff, and J. Schwiening, A 30 ps timing resolution for single photons with multi-pixel Burle MCP-PMT, *Nucl. Instrum. Methods Phys. Res. A* **572**, 459 (2007).
- [37] H. Kume, K. Koyama, K. Nakatsugawa, S. Suzuki, and D. Fatlowitz, Ultrafast microchannel plate photomultipliers, *Appl. Opt.* **27**, 1170 (1988).
- [38] J. H. Posthumus, The dynamics of small molecules in intense laser fields, *Rep. Prog. Phys.* **67**, 623 (2004).
- [39] W. Li, S. A. Lahankar, C. Huang, P. S. Shternin, O. S. Vasyutinskii, and A. G. Suits, Multiphoton processes of CO at 230 nm, *Phys. Chem. Chem. Phys.* **8**, 2950 (2006).
- [40] K. Okada and S. Iwata, Accurate potential energy and transition dipole moment curves for several electronic states of CO^+ , *J. Chem. Phys.* **112**, 1804 (2000).
- [41] T. F. Moran, J. B. Wilcox, and L. E. Abbey, Collision-induced dissociation of CO^+ in $\text{X}^2\Sigma^+$ and metastable states in $\text{CO}^+ - \text{CO}$ interactions, *J. Chem. Phys.* **68**, 261 (1978).
- [42] M. T. Bowers, M. Chau, and P. R. Kemper, Reactions of ions in excited electronic states: $(\text{CO}^+)^* + \text{CO} \rightarrow \text{C}_2\text{O}^+ + \text{CO}$, *J. Chem. Phys.* **63**, 3656 (1975).
- [43] R. Livingston, Review of photosynthesis and related processes. volume ii, part 2. kinetics of photosynthesis, *J. Am. Chem. Soc.* **78**, 6215 (1956).
- [44] R. A. Berner, A new look at the long-term carbon cycle, *GSA Today* **9**, 2 (1999).
- [45] A. Hishikawa, A. Iwamae, and K. Yamanouchi, Ultrafast deformation of the geometrical structure of CO_2 induced in intense laser fields, *Phys. Rev. Lett.* **83**, 1127 (1999).

- [46] Y. Sato, H. Kono, S. Koseki, and Y. Fujimura, Description of molecular dynamics in intense laser fields by the time-dependent adiabatic state approach: application to simultaneous two-bond dissociation of CO₂ and its control, *J. Am. Chem. Soc.* **125**, 8019 (2003).
- [47] I. Bocharova, R. Karimi, E. F. Penka, J.-P. Brichta, P. Lassonde, X. Fu, J.-C. Kieffer, A. D. Bandrauk, I. Litvinyuk, J. Sanderson, and F. m. c. Légaré, Charge resonance enhanced ionization of CO₂ probed by laser coulomb explosion imaging, *Phys. Rev. Lett.* **107**, 063201 (2011).
- [48] C. Wu, C. Wu, D. Song, H. Su, Y. Yang, Z. Wu, X. Liu, H. Liu, M. Li, Y. Deng, Y. Liu, L. Y. Peng, H. Jiang, and Q. Gong, Nonsequential and sequential fragmentation of CO₂³⁺ in intense laser fields, *Phys. Rev. Lett.* **110**, 103601 (2013).
- [49] N. Neumann, D. Hant, L. P. H. Schmidt, J. Titze, T. Jahnke, A. Czasch, M. S. Schöffler, K. Kreidi, O. Jagutzki, H. Schmidt-Böcking, and R. Dörner, Fragmentation dynamics of CO₂³⁺ investigated by multiple electron capture in collisions with slow highly charged ions, *Phys. Rev. Lett.* **104**, 103201 (2010).